

Multi-site mean-field theory for cold bosonic atoms in optical lattices

T. McIntosh, P. Pisarski, R. J. Gooding, and E. Zaremba

*Department of Physics, Engineering Physics, and Astronomy,
Queen's University, Kingston, ON K7L 3N6, Canada*

(Dated: July 27, 2018)

We present a detailed derivation of a multi-site mean-field theory (MSMFT) used to describe the Mott-insulator to superfluid transition of bosonic atoms in optical lattices. The approach is based on partitioning the lattice into small clusters which are decoupled by means of a mean field approximation. This approximation invokes local superfluid order parameters defined for each of the boundary sites of the cluster. The resulting MSMFT grand potential has a non-trivial topology as a function of the various order parameters. An understanding of this topology provides two different criteria for the determination of the Mott insulator superfluid phase boundaries. We apply this formalism to d -dimensional hypercubic lattices in one, two and three dimensions, and demonstrate the improvement in the estimation of the phase boundaries when MSMFT is utilized for increasingly larger clusters, with the best quantitative agreement found for $d = 3$. The MSMFT is then used to examine a linear dimer chain in which the on-site energies within the dimer have an energy separation of Δ . This system has a complicated phase diagram within the parameter space of the model, with many distinct Mott phases separated by superfluid regions.

I. INTRODUCTION

The properties of both the pure and disordered Bose-Hubbard (BH) model were first elucidated in a remarkably insightful paper by Fisher *et al.* [1]. For the case of a pure (or homogeneous) system, it was shown that a collection of interacting bosons on a lattice undergoes a Mott insulator (MI) to superfluid (SF) transition as the ratio J/U is varied, where J characterizes the rate of hopping from one lattice site to another, and U represents the interaction between two bosons residing on a given site. The insulating phase appears as lobes in the μ/U vs. J/U plane, where μ is the chemical potential, within which the average occupancy per site takes on an integral value. Outside these bounded regions, the system is a superfluid characterized by a nonzero condensate order parameter, and the density varies continuously with the system parameters.

The BH model became particularly germane with the advent of trapped Bose gases and Jaksch *et al.* [2] proposed that the model would provide a realistic theoretical description of bosons residing in an optical lattice. They obtained estimates of the parameters appearing in the BH model and argued that the model is relevant to the physical systems experimentally accessible. Subsequent experiments [3] indeed showed that trapped Bose gases are an ideal setting within which to study the theoretically predicted MI-SF transition.

Many theoretical studies of the BH model followed the original Fisher *et al.* paper [1] using a variety of theoretical methods and approximations and the properties of the transition in one, two and three dimensions are now well established [4–11]. Apart from the considerable work done on the disordered BH model [1, 4, 5, 12, 13], the model has also been extended to superlattices [7, 14–22], spinor condensates [23–25], multi-component systems [22, 26–28] and multiband situations [29–31]. With increasing complexity, the MI-SF phase diagram becomes increasingly richer in structure.

One of the most useful theoretical approaches for obtaining a qualitative understanding of the MI-SF transition is mean-field theory which was originally motivated by considering the infinite-range hopping limit [1]. Subsequent reformulations of mean-field theory [32, 33] invoked the existence of a condensate order parameter which was used to decouple the nonlocal hopping term of the BH Hamiltonian. In its simplest form, which we refer to as the site-decoupled mean-field theory (SDMFT), the decoupling leads to a system Hamiltonian consisting of a sum of site Hamiltonians. The latter are effectively independent but depend on the order parameter, in general site-dependent, which can be thought of as a variational parameter. For a homogeneous lattice, the ground state of the system is determined by minimizing the system energy with respect to the order parameter. If the energy is minimized for a non-zero value of the order parameter, the system is in the SF phase, otherwise it is in the MI phase. The phase boundaries obtained using this approach are consistent with the results of more sophisticated approaches. It can be shown [32] that SDMFT is equivalent to the alternative starting point based on the Gutzwiller ansatz for the ground-state wave function [35, 36].

One of the limitations of the SDMFT is the neglect of inter-site correlations which allow for fluctuations of various physical variables. For example, in the MI phase of a homogeneous system, the site occupancy is precisely integral, whereas in reality some (albeit small) fluctuations in the site occupancy must occur. These effects can be captured, at least to some extent, by dividing the system into clusters of arbitrary size and using mean-field theory to decouple the clusters. We refer to theories of this kind as multi-site mean-field theories (MSMFT) and in this paper, explore this

approximation for various situations. This approach has been used previously by Buonsante *et al.* [15, 17] to study the MI-SF transition in superlattices where novel (loophole) features emerge and in an investigation of the disorderd BH model [13]. It should be noted that a two-site mean-field theory was also introduced in [37] using the so-called phase-space method.

The main purpose of this paper is to provide a detailed derivation of the MSMFT and to explain how it can be used to systematically improve the quality of the results for the MI-SF phase boundary. It should be emphasized at the outset that the method cannot compete in a quantitative sense with more sophisticated methods such as quantum Monte Carlo (QMC) [4, 7–9], the density-matrix renormalization-group (DMRG) method [6, 25] and other theoretical techniques [5, 11]. However, the MSMFT method is relatively straightforward and allows one to explore efficiently the dependence of its predictions on the various parameters which define more complex physical models. In addition, as stated earlier, it has the merit of providing useful information about inter-site correlations that are missed in the SDMFT.

Our paper is organized as follows. In Sec. II A we derive the MSMFT for the simplest case of a one-dimensional lattice where the definition of clusters used in the multi-site decoupling is particularly straightforward. The method is extended in Sec. II B to higher dimensions where more freedom is available, within certain limits, in defining the clusters which cover the lattice. The MI-SF transition is determined by means of a grand potential which is a function of the various superfluid order parameters defined for the cluster. A detailed analysis of the grand potential leads to two different criteria for the determination of the phase boundaries. Our results for the case of homogeneous lattices are presented in Sec. III. In Sec. IV we consider one-dimensional superlattices; the simplest consists of alternating *A* and *B* sites which we refer to as a dimer chain. In this case, the nonequivalence of the sites requires two different order parameters for the description of the superfluid phase. We also consider an example of a four-site superlattice where qualitative differences appear in the predictions of SDMFT and MSMFT.

II. FORMALISM: MULTI-SITE MEAN-FIELD THEORY

A. Derivation in One Dimension

Our work is based on the BH Hamiltonian [2] in the grand canonical ensemble. With the assumption of a single orbital per site, this Hamiltonian is given by

$$\hat{\mathcal{K}} = \hat{\mathcal{H}} - \mu \hat{\mathcal{N}} = \sum_i (\varepsilon_i - \mu) \hat{n}_i + \frac{1}{2} \sum_i U_i \hat{n}_i (\hat{n}_i - 1) - \sum_{ij} J_{ij} \hat{c}_i^\dagger \hat{c}_j, \quad (1)$$

where the index *i* labels the sites of the optical lattice and \hat{c}_i^\dagger and \hat{c}_i are site creation and annihilation operators (henceforth referred to as site operators), respectively; the number operator for site *i* is given by $\hat{n}_i = \hat{c}_i^\dagger \hat{c}_i$. The system parameters include the on-site energies ε_i at each lattice site, the tunnelling energy J_{ij} between sites *i* and *j*, and the intra-site interaction energy U_i . To a good approximation it is sufficient to ignore interactions between bosons on different sites and hopping between sites further apart than the nearest-neighbour distance [2, 38]. Furthermore, we will restrict our considerations to the case where the interaction parameter has a common value U for all sites and a hopping parameter J for all nearest-neighbour pairs. Generalizations to more complex situations such as superlattices [15–17] can be readily accommodated in the MSMFT that we develop. The final parameter in the BH Hamiltonian is the chemical potential μ which controls the number of particles in the system. Although extensions to finite temperatures are certainly feasible [16], we will only consider the properties of the BH Hamiltonian at zero temperature.

The MSMFT [15] is most easily formulated for the example of a homogeneous one-dimensional chain with nearest-neighbour hopping. The on-site energies ε_i can be set to zero and the interactions are taken to be site independent. The first step in the derivation is to partition a chain having N_s sites into N_c clusters each containing L sites, so that

$$N_s = L N_c. \quad (2)$$

We will refer to the cluster of length L as an “ L -mer”. A schematic of the partitioning being considered is shown in Fig. 1. The hopping part of the Hamiltonian, $\hat{\mathcal{H}}_{hop} = -J \sum_{\langle ij \rangle} \hat{c}_i^\dagger \hat{c}_j$, can then be written as

$$\hat{\mathcal{H}}_{hop} = -J \sum_{j=0}^{N_c-1} \sum_{l=1}^{L-1} (\hat{c}_{Lj+l}^\dagger \hat{c}_{Lj+l+1} + \hat{c}_{Lj+l+1}^\dagger \hat{c}_{Lj+l}) - J \sum_{j=0}^{N_c-1} (\hat{c}_{Lj+L}^\dagger \hat{c}_{Lj+L+1} + \hat{c}_{Lj+L+1}^\dagger \hat{c}_{Lj+L}). \quad (3)$$

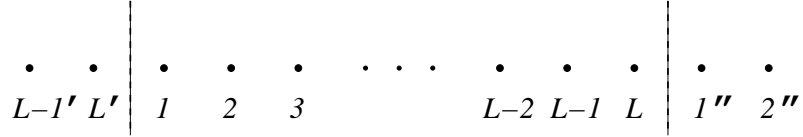


FIG. 1: The partitioning of a one-dimensional chain into linear clusters of length L . Within our multi-site mean-field formulation each cluster with open boundary conditions is treated exactly, and the inter-cluster couplings (generated by the hopping Hamiltonian) are treated in a mean-field decoupling approximation.

where we have isolated the terms with $l = L$ in the second sum which couple sites between adjacent L -mers. This term will be denoted by $\hat{\mathcal{H}}_{coup}$. We assume periodic boundary conditions so that $\hat{c}_{LN_c+1} \equiv \hat{c}_1$.

The coupling between L -mers can be eliminated by invoking the usual argument [32, 33]. We assume the existence of a homogenous superfluid order parameter

$$\psi = \langle \hat{c}_i \rangle, \quad (4)$$

and write $\hat{c}_i = \psi + (\hat{c}_i - \psi)$ for each of the operators in $\hat{\mathcal{H}}_{coup}$. Neglecting quadratic terms in the fluctuation $\delta\hat{c}_i = \hat{c}_i - \psi$, we find

$$\hat{\mathcal{H}}_{coup} \simeq -J \sum_{j=0}^{N_c-1} \left[(\hat{c}_{Lj+L}^\dagger + \hat{c}_{L(j+1)+1}^\dagger) \psi + (\hat{c}_{Lj+L} + \hat{c}_{L(j+1)+1}) \psi^* \right] + 2JN_c |\psi|^2 \quad (5)$$

We thus arrive at the cluster-decoupled Hamiltonian

$$\hat{\mathcal{K}} = \sum_{j=0}^{N_c-1} \hat{\mathcal{K}}_j^{MF}, \quad (6)$$

where $\hat{\mathcal{K}}_j^{MF}$ only depends on the site operators within the j -th L -mer. Taking $j = 0$, we have

$$\hat{\mathcal{K}}_0^{MF} = \hat{\mathcal{K}}_L^0 + \hat{\mathcal{V}}_L^{MF}, \quad (7)$$

where

$$\hat{\mathcal{K}}_L^0 = \frac{U}{2} \sum_{l=1}^L \hat{n}_l (\hat{n}_l - 1) - \mu \sum_{l=1}^L \hat{n}_l - J \sum_{l=1}^{L-1} (\hat{c}_l^\dagger \hat{c}_{l+1} + \hat{c}_{l+1}^\dagger \hat{c}_l), \quad (8)$$

and

$$\hat{\mathcal{V}}_L^{MF} = -J \left[\psi (\hat{c}_1^\dagger + \hat{c}_L^\dagger) + \psi^* (\hat{c}_1 + \hat{c}_L) \right] + 2J |\psi|^2. \quad (9)$$

The ψ -independent operator $\hat{\mathcal{K}}_L^0$ is the Hamiltonian of a one-dimensional chain of length L with open ends. The different L -mers are independent physical systems but are effectively coupled by means of the order parameter appearing in the mean-field perturbation $\hat{\mathcal{V}}_L^{MF}$.

It is clear from the form of (9) that the phase of the order parameter, $\psi = |\psi| \exp(i\phi)$, can be absorbed by a redefinition of the site operators: $\exp(-i\phi)\hat{c}_l \rightarrow \hat{c}_l$. The resulting Hamiltonian depends on $|\psi|$ and we can therefore take the order parameter ψ to be a real, positive quantity. The ground state of the system described by a single homogeneous order parameter can be determined by minimizing $\hat{\mathcal{K}}_0^{MF}$ with respect to ψ in the L -mer Fock space.

B. MSMFT in Higher Dimensions

The extension of the MSMFT to higher dimensions is straightforward, although some new elements appear due to the freedom available in partitioning the lattice into clusters. This is illustrated in Fig. 2(a) for the example of a two-dimensional square lattice. The figure shows how the lattice can be covered using L -mers with size $L = 1, 2, 4, 5$ and 6. It is clearly necessary that these clusters cover the entire lattice without duplication. It is also desirable that they have the same point-group symmetry as the original lattice. The examples $L = 1, 4$ and 9 satisfy this latter

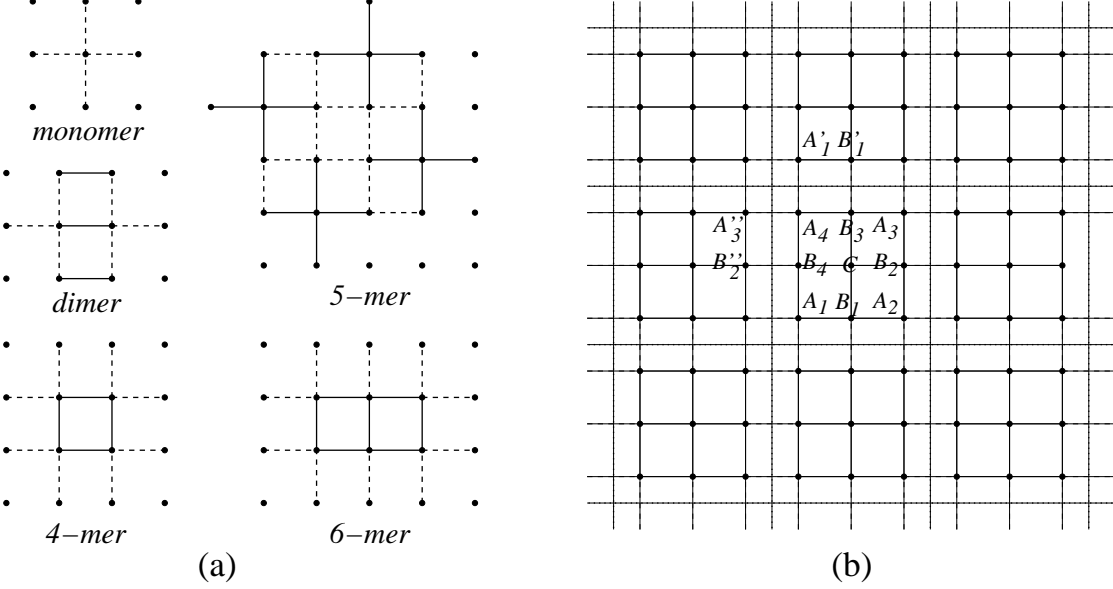


FIG. 2: The partitioning of a two-dimensional square lattice using various repeated clusters. Shown in (a) are single site monomers, dimers ($L = 2$), and L -mers for $L = 4, 5, 6$. Shown in (b) is a portion of a two-dimensional square lattice that is partitioned into 3×3 clusters. The solid lines connect sites in a given cluster, dotted lines show the division of the lattice into such clusters, and the dashed lines show the inter-cluster couplings that are treated within mean-field theory. In each cluster there are three inequivalent sites: the central site C , which does not couple to neighbouring clusters, and corner and edge sites, which respectively are labelled A and B .

criterion. The $L = 5$ cluster has the point-group symmetry of the square lattice, but its covering of the 2D plane introduces a chirality not present in the homogeneous system.

Although we develop the MSMFT in its most general form, it will be useful to keep in mind the example of a two-dimensional square lattice with the 3×3 clusters shown in Fig. 2(b). The sites in the lattice can be specified by $\mathbf{R} + \boldsymbol{\tau}$, where \mathbf{R} is a cluster Bravais lattice vector and $\boldsymbol{\tau}$ defines the basis of sites within the cluster. For the example of Fig. 2(b), $\boldsymbol{\tau}$ runs over the nine sites of the 3×3 clusters. A site on the boundary of a cluster will be denoted by α and is connected, via J , to one or more boundary sites on adjacent clusters. The mean-field decoupling of the hopping term for the boundary site α in the L -mer and the boundary site β' of the adjoining L' -mer is achieved using the prescription

$$\hat{c}_\alpha^\dagger \hat{c}_{\beta'} + \hat{c}_{\beta'}^\dagger \hat{c}_\alpha \rightarrow \psi_\beta \hat{c}_\alpha^\dagger + \psi_\beta^* \hat{c}_\alpha + \psi_\alpha \hat{c}_{\beta'}^\dagger + \psi_\alpha^* \hat{c}_{\beta'} - \psi_\alpha^* \psi_\beta - \psi_\alpha \psi_\beta^*. \quad (10)$$

In general, we allow for different order parameters for each of the boundary sites. Since the β' site in the L' -mer is related to the β site in the L -mer by translational symmetry, we have denoted the order parameter on this site as ψ_β . (For example, the sites A'_1 and A_1 in Fig. 2(b) must have the same order parameter by translational symmetry.) For now, we have also allowed the order parameters to be complex. Collecting all terms pertaining to the L -mer, the mean-field decoupling leads to the L -mer mean-field perturbation

$$\hat{\mathcal{V}}_L^{MF}(\{\psi_\alpha\}) \equiv - \sum_{\alpha\beta} J_{\alpha\beta} (\hat{c}_\alpha^\dagger \psi_\beta + \hat{c}_\alpha \psi_\beta^* - \psi_\alpha^* \psi_\beta), \quad (11)$$

where the sums extend over all boundary sites. To obtain this form we have defined the symmetric matrix \underline{J} with matrix elements $J_{\alpha\beta} \equiv J g_{\alpha\beta}$ where $g_{\alpha\beta}$ is the number of clusters to which the L -mer of interest is connected by a pair of α and β sites in the way described above. If such a pair of sites is not coupled, $g_{\alpha\beta} = 0$. We will refer to \underline{J} as the *connectivity* matrix, since it encapsulates the way in which the different sites in the cluster are connected to one another via the mean-field couplings [34].

The perturbation in (11) depends on the set of order parameters $\{\psi_\alpha\}$ defined for the ensemble of boundary sites. The cluster Hamiltonian then takes the general form

$$\hat{\mathcal{K}}^{MF}(\{\psi_\alpha\}) = \hat{\mathcal{K}}_L^0 + \hat{\mathcal{V}}_L^{MF}(\{\psi_\alpha\}), \quad (12)$$

where the ψ_α -independent part

$$\hat{\mathcal{K}}_L^0 = \frac{U}{2} \sum_{l=1}^L \hat{n}_l (\hat{n}_l - 1) + \sum_{l=1}^L (\varepsilon_l - \mu) \hat{n}_l - J \sum_{\langle lm \rangle} \hat{c}_l^\dagger \hat{c}_m, \quad (13)$$

is the sum of terms in the grand canonical Hamiltonian $\hat{\mathcal{K}}$ that depend only on the L -mer variables. The final sum in (13) is restricted to nearest-neighbour pairs within the L -mer. It is important to note that this intra-cluster hopping leads to inter-site correlations even within the Mott insulating phase.

The MSMFT Hamiltonian depends on various factors, such as the dimension and geometry of the lattice, the shape and size of the clusters and the coordination of sites in one cluster with those of its neighbours. The extent to which different order parameters are required depends on the physical application and will be clarified by example. However, we emphasize that these order parameters are not prescribed but in general are determined by the solution of the mean-field problem itself.

The cluster grand canonical Hamiltonian (12) is Hermitian but it is not number-conserving due to the perturbation in (11). As a result, its eigenvectors must be determined in the L -mer Fock space. We denote the state with the lowest eigenvalue $\Omega_0(\{\psi_\alpha\})$ as $|\Psi_0\rangle$. For a normalized state vector, the variation of $\Omega_0(\{\psi_\alpha\})$ with respect to ψ_γ^* is given by

$$\frac{\partial \Omega_0(\{\psi_\alpha\})}{\partial \psi_\gamma^*} = \left\langle \Psi_0 \left| \frac{\partial \hat{\mathcal{V}}_L^{MF}(\{\psi_\alpha\})}{\partial \psi_\gamma^*} \right| \Psi_0 \right\rangle = - \sum_{\alpha} J_{\alpha\gamma} \langle \Psi_0 | \hat{c}_\alpha - \psi_\alpha | \Psi_0 \rangle. \quad (14)$$

This implies that $\Omega_0(\{\psi_\alpha\})$ is stationary when the order parameters satisfy

$$\langle \hat{c}_\gamma \rangle \equiv \langle \Psi_0(\{\bar{\psi}_\alpha\}) | \hat{c}_\gamma | \Psi_0(\{\bar{\psi}_\alpha\}) \rangle = \bar{\psi}_\gamma \quad (15)$$

for all boundary sites γ , where the values of the order parameters at the stationary point are denoted by $\bar{\psi}_\gamma$. We thus see that stationarity of the grand potential is associated with the physically necessary condition that the order parameters are determined self-consistently. If more than one stationary point arises, the physical state of the system is assumed to correspond to the stationary point with the minimum value of $\Omega_0(\{\bar{\psi}_\alpha\})$.

Intuition might lead one to expect that a stationary point is an extremum of the grand potential, but it is straightforward to show that it is *not*. Writing $\psi_\alpha = \bar{\psi}_\alpha + \Delta\psi_\alpha$ and expanding (12) about a stationary point, we have

$$\hat{\mathcal{K}}^{MF}(\{\psi_\alpha\}) = \hat{\mathcal{K}}^{MF}(\{\bar{\psi}_\alpha\}) - \sum_{\alpha\beta} J_{\alpha\beta} [(\hat{c}_\alpha^\dagger - \bar{\psi}_\alpha^*) \Delta\psi_\beta + (\hat{c}_\alpha - \bar{\psi}_\alpha) \Delta\psi_\beta^* - \Delta\psi_\alpha^* \Delta\psi_\beta]. \quad (16)$$

We denote the sum by $\Delta\hat{\mathcal{V}}_L^{MF}$ and consider it as a perturbation to the grand Hamiltonian $\hat{\mathcal{K}}^{MF}(\{\bar{\psi}_\alpha\})$ at the stationary point. The first order correction to the grand potential $\Omega_0(\{\bar{\psi}_\alpha\})$ is

$$\Omega_0^{(1)}(\{\Delta\psi_\alpha\}) = \langle \Psi_0 | \Delta\hat{\mathcal{V}}_L^{MF} | \Psi_0 \rangle = \sum_{\alpha\beta} J_{\alpha\beta} \Delta\psi_\alpha^* \Delta\psi_\beta \quad (17)$$

while the second order correction is

$$\Omega_0^{(2)}(\{\Delta\psi_\alpha\}) = \sum_{\nu \neq 0} \frac{|\langle \nu | \sum_{\alpha\beta} J_{\alpha\beta} [\hat{c}_\alpha^\dagger \Delta\psi_\beta + \hat{c}_\alpha \Delta\psi_\beta^*] | 0 \rangle|^2}{\Omega_0(\{\bar{\psi}_\alpha\}) - \Omega_\nu(\{\bar{\psi}_\alpha\})}, \quad (18)$$

where the states $|\nu\rangle$ are eigenstates of $\hat{\mathcal{K}}^{MF}(\{\bar{\psi}_\alpha\})$ with eigenvalues $\Omega_\nu(\{\bar{\psi}_\alpha\})$. $\Omega_0^{(2)}$ is negative definite and $\Omega_0^{(1)}$ can always be made negative by choosing $\Delta\psi_\beta = -\Delta\psi_\alpha$ for some pair of deviations with all others equal to zero. Thus, unlike the situation for the case of a single order parameter, a stationary point is not a local minimum; the value of $\Omega_0(\{\psi_\alpha\})$ can always be made smaller than $\Omega_0(\{\bar{\psi}_\alpha\})$ by moving away from the stationary point in some direction. For multiple order parameters, the stationary point is, in general, a saddle point and as a result, it cannot be located by means of a variational principle. Below, we provide criteria for identifying the emergence of a superfluid phase from a Mott insulating phase without having to appeal to a variational principle.

C. Perturbative Treatment of the MI-SF Transition

The point $\{\psi_\alpha\} = \{0\}$ is always a stationary point and it too is not an extremum in general. This point has special significance in that it corresponds to the Mott insulating phase. Assuming the MI-SF transition to be continuous

as a function of the system parameters (for example, the hopping strength J), we expect the stationary point to move continuously away from the $\{\psi_\alpha\} = \{0\}$ point as the parameters are varied beyond some critical values. This behaviour can be analyzed by treating (11) as a perturbation to $\hat{\mathcal{K}}_L^0$. Depending on the values of the system parameters (μ , J and U), $\hat{\mathcal{K}}_L^0$ has a ground state $|0\rangle$ containing N particles. The range of parameters for which this is the case defines what we refer to as N -domains in the multi-dimensional parameter space. Each of these N -domains can, in principle, give rise to a Mott phase with a certain number of particles per cluster. These regions are conventionally referred to as Mott lobes.

The first and second order corrections to the energy $\Omega_0(\{0\})$ are obtained with the replacement $\bar{\psi}_\alpha \rightarrow 0$ and $\Delta\psi_\alpha \rightarrow \psi_\alpha$ in (17) and (18). We have

$$\Omega_0^{(1)}(\{\psi_\alpha\}) = \sum_{\alpha\beta} J_{\alpha\beta} \psi_\alpha^* \psi_\beta \quad (19)$$

and

$$\Omega_0^{(2)}(\{\psi_\alpha\}) = \sum_{\nu \neq 0} \frac{|\langle \nu | \sum_{\alpha\beta} J_{\alpha\beta} [\hat{c}_\alpha^\dagger \psi_\beta + \hat{c}_\alpha \psi_\beta^*] |0\rangle|^2}{\Omega_0(\{0\}) - \Omega_\nu(\{0\})}, \quad (20)$$

where in this case, the states $|\nu\rangle$ are eigenstates of $\hat{\mathcal{K}}_L^0$ and are therefore number eigenstates. For the matrix elements in the sum to be nonzero, the state $|\nu\rangle$ must have either $N - 1$ or $N + 1$ particles. Defining the operator

$$\hat{O}_\alpha = \sum_\beta J_{\alpha\beta} \hat{c}_\beta, \quad (21)$$

we see that the second order correction is given by

$$\Omega_0^{(2)}(\{\psi_\alpha\}) = \sum_{\alpha\beta} M_{\alpha\beta} \psi_\alpha^* \psi_\beta \quad (22)$$

where the Hermitian matrix \underline{M} is defined by

$$M_{\alpha\beta} = \sum_{\nu \neq 0} \frac{\langle 0 | \hat{O}_\alpha | \nu \rangle \langle \nu | \hat{O}_\beta^\dagger | 0 \rangle + \langle 0 | \hat{O}_\beta^\dagger | \nu \rangle \langle \nu | \hat{O}_\alpha | 0 \rangle}{\Omega_0(\{0\}) - \Omega_\nu(\{0\})}. \quad (23)$$

In obtaining this result we have used the fact that the operator \hat{O}_α only has finite matrix elements between states whose particle numbers differ by one. In view of (21), we see that

$$\underline{M} = \underline{J} \underline{C} \underline{J} \quad (24)$$

where the elements of the Hermitian matrix \underline{C} are given by

$$C_{\alpha\beta} = \sum_{\nu \neq 0} \frac{\langle 0 | \hat{c}_\alpha | \nu \rangle \langle \nu | \hat{c}_\beta^\dagger | 0 \rangle + \langle 0 | \hat{c}_\beta^\dagger | \nu \rangle \langle \nu | \hat{c}_\alpha | 0 \rangle}{\Omega_0(\{0\}) - \Omega_\nu(\{0\})}. \quad (25)$$

Combining (19) and (22), we have

$$\Omega_0(\{\psi_\alpha\}) = \Omega_0(\{0\}) + \sum_{\alpha\beta} W_{\alpha\beta} \psi_\alpha^* \psi_\beta + \dots, \quad (26)$$

where

$$\underline{W} \equiv \underline{J} + \underline{M} = \underline{J} + \underline{J} \underline{C} \underline{J}. \quad (27)$$

We will refer to the Hermitian matrix \underline{W} as the energy matrix.

If the value $\Omega_0(\{0\})$ is the minimum of all stationary points, one is in the Mott insulating phase. The question then arises as to whether the stability of the Mott phase can be established independently of determining $\Omega_0(\{\psi_\alpha\})$

for all of these points. Since $\Omega_0(\{0\})$ is not an extremum, it is not obvious *a priori* what properties the energy matrix \underline{W} must have in order for the Mott phase to be stable. To address this query we determine the eigenvectors and eigenvalues of \underline{W} :

$$\underline{W} \mathbf{v}_i = \omega_i \mathbf{v}_i. \quad (28)$$

Since \underline{W} is Hermitian, the eigenvalues are real and the eigenvectors can be chosen to be an orthonormal set. Expanding the order-parameter vector $\psi \equiv \{\psi_\alpha\}$ as

$$\psi = \sum_i \xi_i \mathbf{v}_i, \quad (29)$$

we see that

$$\Delta\Omega_0(\psi) = \sum_i \omega_i |\xi_i|^2. \quad (30)$$

The eigenvectors \mathbf{v}_i thus define directions in the order-parameter space along which the grand potential varies quadratically with a curvature that is determined by the sign of ω_i . Furthermore, as one moves along a line in one of these directions, the grand potential is stationary with respect to displacements away from the line. Thus the transition to the SF phase must be accompanied by the appearance of a stationary point with $\psi \neq \mathbf{0}$ along one of these directions. The only scenario consistent with the continuous movement of the stationary point away from $\psi = \mathbf{0}$ is that one of the positive eigenvalues passes through zero. The first positive eigenvalue to do so establishes the criterion for the transition to the SF phase. This is very analogous to the situation one finds with a single order parameter [33]. We elaborate on these properties of the grand potential below, and illustrate the general behaviour with a concrete numerical example in Sec. II E.

We now denote the vector relevant to the transition as \mathbf{v}_1 . When ω_1 passes through zero, the stationary point moves continuously from $\psi = \mathbf{0}$ to a point where the order parameter is non-zero. If higher order terms in the perturbation expansion are retained, one expects the grand potential to behave, in the vicinity of the transition, according to the Landau theory [39] expression

$$\Delta\Omega_0(\psi) = \frac{r}{2} |\xi_1|^2 + \frac{u}{4} |\xi_1|^4, \quad (31)$$

where $r = 2\omega_1$, and we assume u to be positive. For small and negative ω_1 , this leads to the stationary order parameter

$$\psi = \sqrt{\frac{|r|}{u}} \mathbf{v}_1. \quad (32)$$

Since the vector \mathbf{v}_1 can be chosen to be a real, one sees that, in the vicinity of the phase boundary, the order parameter is real. In other words, there are no phase differences (apart from a possible sign) between the order parameter components. In fact, in all the examples we have studied, the components of the order parameter vector all have the *same* sign, which we take to be positive. One might argue that this is the expected behaviour, since relative sign differences in the components would lead to more rapid spatial variations of the order parameter with a resultant higher kinetic energy. However, as stated earlier, the grand potential is not an extremum at the stationary point and can take on lower values if one moves away from the stationary point in some direction \mathbf{v}_i . Since this vector is orthogonal to \mathbf{v}_1 , it must necessarily have components with different signs. One therefore cannot argue that the components of the physically relevant direction (\mathbf{v}_1) must have the same sign on the basis of energy considerations. Henceforth, we assume that the components of the order parameter are real. This assumption is supported by all self-consistent solutions of (12) that we have obtained in the SF phase.

Referring to Eq. (27), we see that the eigenvalue spectrum of \underline{W} is closely related to that of the connectivity matrix \underline{J} . In fact, for $J \rightarrow 0$, the eigenvectors and eigenvalues of these two matrices coincide. The eigenvectors of \underline{J} are defined by

$$\underline{J} \mathbf{u}_i = \lambda_i \mathbf{u}_i. \quad (33)$$

The eigenvectors with zero eigenvalue play a special role in that they are simultaneously zero-eigenvalue eigenvectors of \underline{W} . These vectors are independent of the magnitude of J and other system parameters, and are simply determined

by the structure of \underline{J} . The eigenvectors of \underline{W} with non-zero eigenvalues can be determined by using \mathbf{u}_i as the basis vectors. Then, in what we call the J -representation, we have

$$W_{ij}^{(J)} = \lambda_i \delta_{ij} + \lambda_i C_{ij}^{(J)} \lambda_j. \quad (34)$$

If we order the $\lambda_i = 0$ eigenvectors as $i = 1, \dots, m$ and the remaining n eigenvectors as $i = m+1, \dots, m+n$, the non-zero eigenvectors of \underline{W} are found in the n -dimensional subspace spanned by the eigenvectors of \underline{J} with non-zero eigenvalues, and are determined by

$$\det \left(W_{n \times n}^{(J)} - \omega I_{n \times n} \right) = 0. \quad (35)$$

Here we have defined the $n \times n$ matrix

$$W_{n \times n}^{(J)} = D_{n \times n} + D_{n \times n} C_{n \times n}^{(J)} D_{n \times n} \quad (36)$$

where $D_{n \times n}$ is the diagonal matrix

$$D_{n \times n} = \begin{pmatrix} \lambda_{m+1} & 0 & \cdots & 0 \\ 0 & \lambda_{m+2} & & \vdots \\ \vdots & & \ddots & 0 \\ 0 & \cdots & 0 & \lambda_{m+n} \end{pmatrix}, \quad (37)$$

and

$$C_{n \times n}^{(J)} = \begin{pmatrix} C_{m+1,m+1}^{(J)} & \cdots & C_{m+1,m+n}^{(J)} \\ \vdots & \ddots & \vdots \\ C_{m+n,m+1}^{(J)} & \cdots & C_{m+n,m+n}^{(J)} \end{pmatrix}. \quad (38)$$

The MI-SF transition is located by following the eigenvalues determined by (35) as a function of a system parameter, such as J . As discussed above, the positive eigenvalue ω_1 which first passes through zero determines the phase boundary. In view of (35), the condition for this to happen is $\det(W_{n \times n}^{(J)}) = 0$.

Although the eigenvalue problem in (35) eliminates the eigenvectors with zero eigenvalues, in practice it is more straightforward to determine all the eigenvalues and eigenvectors using (28). When the ω_1 eigenvalue is identified and found to pass through zero, the corresponding eigenvector directly determines the relative magnitude of the order parameter components just as one enters the SF phase. The main advantage of the J -representation is that it reveals the mathematical structure of the \underline{W} matrix and facilitates some of the formal developments that follow.

An alternate approach to that of following the \underline{W} eigenvalues is based on constructing a stability criterion for the Mott phase [17]. It too is based on a perturbative analysis and can be derived as follows. To first order in perturbation theory, one finds that

$$\langle \hat{c}_\alpha \rangle^{(1)} = \sum_\beta S_{\alpha\beta} \psi_\beta, \quad (39)$$

where the matrix \underline{S} , which we refer to as the stability matrix, is defined in terms of matrices introduced earlier, namely

$$\underline{S} = -\underline{C} \underline{J}. \quad (40)$$

We note that this matrix is *not* Hermitian. Since the left-hand side of Eq. (39) is the perturbative estimate of ψ_α , this equation is suggestive of an iterative scheme defined by the linear map

$$\psi_\alpha^{(k+1)} = \sum_\beta S_{\alpha\beta} \psi_\beta^{(k)}, \quad (41)$$

where $k = 0, 1, 2, \dots$ can be thought of as an iteration index with $k \rightarrow \infty$ identifying the self-consistent solution. Defining the eigenvectors of \underline{S} by

$$\underline{S} \mathbf{z}_i = \sigma_i \mathbf{z}_i, \quad (42)$$

we see that the iterative sequence converges to the Mott insulating $\psi = \mathbf{0}$ fixed point if the absolute values of the eigenvalues σ_i are all less than one. Therefore, this procedure provides an operational definition of the Mott phase in terms of the eigenvalues of the stability matrix \underline{S} .

The definition of the stability matrix in (40) shows that the eigenvectors of \underline{J} with zero eigenvalues are also zero-eigenvalue eigenvectors of \underline{S} , that is, $\mathbf{z}_i = \mathbf{u}_i$ for $i = 1, \dots, m$, with $\sigma_i = 0$. In the J -representation, the stability matrix thus has the block structure

$$\underline{S}^{(J)} = \begin{pmatrix} O_{m \times m} & S_{m \times n}^{(J)} \\ O_{n \times m} & S_{n \times n}^{(J)} \end{pmatrix}, \quad (43)$$

where the null matrices (O) have the dimensions indicated,

$$S_{n \times n}^{(J)} = -C_{n \times n}^{(J)} D_{n \times n} \quad (44)$$

and

$$S_{m \times n}^{(J)} = \begin{pmatrix} -C_{1,m+1}^{(J)} \lambda_{m+1} & \cdots & -C_{1,m+n}^{(J)} \lambda_{m+n} \\ \vdots & \ddots & \vdots \\ -C_{m,m+1}^{(J)} \lambda_{m+1} & \cdots & -C_{m,m+n}^{(J)} \lambda_{m+n} \end{pmatrix}. \quad (45)$$

It is clear from (43) that the $\sigma = 0$ eigenvalue is m -fold degenerate and that the remaining eigenvalues of \underline{S} are determined by the equation

$$\det(S_{n \times n}^{(J)} - \sigma I_{n \times n}) = 0. \quad (46)$$

If these latter eigenvalues all have a magnitude less than one, then $\psi = \mathbf{0}$ is a fixed point of the map defined in (41), and the Mott phase is stable.

The complete set of eigenvectors of \underline{S} consist of the m zero-eigenvalue eigenvectors of \underline{J} together with the remaining n eigenvectors determined by considering the n -dimensional eigenvalue problem

$$S_{n \times n}^{(J)} \mathbf{y}_i = \sigma_i \mathbf{y}_i. \quad (47)$$

In view of (44), this equation is equivalent to the generalized eigenvalue problem

$$C_{n \times n}^{(J)} \mathbf{y}'_i = -\sigma_i D_{n \times n}^{-1} \mathbf{y}'_i, \quad (48)$$

where $\mathbf{y}'_i \equiv D_{n \times n} \mathbf{y}_i$. Since $C_{n \times n}^{(J)}$ is Hermitian and $D_{n \times n}^{-1}$ (the inverse of (37)) is a real diagonal matrix, it is easy to show that the eigenvalues σ_i are real. In addition, for distinct eigenvalues, we have the orthogonality relation $(D_{n \times n} \mathbf{y}_j)^T \mathbf{y}_j = 0$. Once the vectors \mathbf{y}_i have been determined, the $\underline{S}^{(J)}$ eigenvectors for $i = m + 1, \dots, m + n$ are given by

$$\mathbf{z}_i = \begin{pmatrix} \mathbf{x}_i \\ \mathbf{y}_i \end{pmatrix}, \quad (49)$$

with $\mathbf{x}_i = \sigma_i^{-1} S_{m \times n}^{(J)} \mathbf{y}_i$.

We now establish the connection between the two different criteria derived above. The energy and stability matrices are related by

$$\underline{W} = \underline{J}(\underline{I} - \underline{S}). \quad (50)$$

An explicit expression for \underline{S} cannot be obtained from this equation since \underline{J} does not in general have an inverse. However, within the J -representation, we have the more useful relation

$$W_{n \times n}^{(J)} = D_{n \times n} (I_{n \times n} - S_{n \times n}^{(J)}). \quad (51)$$

Since $D_{n \times n}$ has an inverse, we can write

$$S_{n \times n}^{(J)} = I_{n \times n} - D_{n \times n}^{-1} W_{n \times n}^{(J)}. \quad (52)$$

From this we see that an eigenvector $(q_{m+1}, \dots, q_{m+n})^T$ of $W_{n \times n}^{(J)}$ with zero eigenvalue is an eigenvector of $S_{n \times n}^{(J)}$ with eigenvalue one. This particular zero eigenvalue of the \underline{W} matrix is obtained at the critical values of the system parameters and the corresponding eigenvector, previously denoted by \mathbf{v}_1 , is given by $\mathbf{v}_1 = \sum_{i=m+1}^{m+n} q_i \mathbf{u}_i$. Using the structure of the $\underline{S}^{(J)}$ eigenvectors in (49), we thus see that

$$\underline{S} \mathbf{v}_1 = \mathbf{v}_1, \text{ when } \underline{W} \mathbf{v}_1 = 0. \quad (53)$$

We have thus proved that the energy and stability criteria for the transition to the SF phase are equivalent and can therefore be used interchangeably.

D. Self-Consistent Superfluid Solutions

The previous subsection outlined two different algorithms for identifying the parameter values of the Bose-Hubbard model for which the MI phase is stable, and an example of the application of these methods is presented in the next subsection. When the MI phase loses stability, the $T = 0$ ground state of the Bose-Hubbard model corresponds to a superfluid state. The order parameter is then determined by finding the ground state solution of (12) which satisfies the self-consistency condition given by (15).

It is a simple matter to obtain such self-consistent solutions numerically. The iterative map

$$\psi_\gamma^{(k+1)} = \langle \Psi_0(\{\psi_\alpha^{(k)}\}) | \hat{c}_\gamma | \Psi_0(\{\psi_\alpha^{(k)}\}) \rangle \quad (54)$$

provides updated order parameter components in terms of their current values. We find that any initial guess of the order parameters, provided that they all have the same sign, converges to a unique self-consistent solution without the need for special mixing [40] or more advanced techniques. This iterative method was used extensively in a recent paper [13] on disordered systems where a large number of sites with different order parameters are required. For homogeneous systems with only one order parameter, Brent's algorithm for root finding is particularly successful [41].

E. Example Calculation

We now illustrate the calculation of the phase boundary and superfluid order parameters using the methods outlined in the previous two subsections. It is instructive to consider the 2D square lattice partitioned into 3×2 clusters with the site labelling indicated in Fig. 3. For this L -mer, there are six boundary sites: the four corner (A) sites and the two edge (B) sites. The choice of this particular cluster is useful for a number of reasons. First, it demonstrates that meaningful physical results can be obtained even though the cluster does not have the symmetry of the two-dimensional square lattice. Second, it is a relatively simple example with several order parameters which illustrates the general formalism and the structure of the solutions. And lastly, it has obvious symmetries which allow us to reduce the number of independent order parameters; here there end up being two, one for the corner sites and one for the edge sites. Thus, for demonstration purposes this is an ideal cluster to examine.

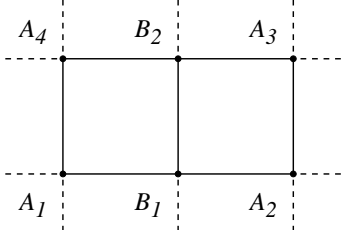


FIG. 3: The partitioning of the two-dimensional square lattice into 3×2 clusters. The cluster consists of inequivalent corner (A) and edge (B) sites.

The calculation of the MI-SF phase boundary can be approached in terms of the energy or stability criterion, each of which involves the connectivity matrix \underline{J} . For the site labelling shown in Fig. 3 and the order parameter specified as $\psi = (\psi_{A_1}, \psi_{A_2}, \psi_{A_3}, \psi_{A_4}, \psi_{B_1}, \psi_{B_2})^T$, the connectivity matrix is given by

$$\underline{J} = \begin{pmatrix} 0 & J & 0 & J & 0 & 0 \\ J & 0 & J & 0 & 0 & 0 \\ 0 & J & 0 & J & 0 & 0 \\ J & 0 & J & 0 & 0 & 0 \\ 0 & 0 & 0 & 0 & 0 & J \\ 0 & 0 & 0 & 0 & J & 0 \end{pmatrix}. \quad (55)$$

We observe that the matrix is block diagonal reflecting the fact that corner sites are coupled to corner sites, and edge sites are coupled to edge sites. Following the notation of (33), the \underline{J} matrix has two $\lambda = 0$ eigenvalues, and the non-zero eigenvalues are $\pm J$ and $\pm 2J$. The energy (27) and stability (40) matrices also depend on the \underline{C} matrix in (25). The evaluation of this matrix requires the eigenstates $|\nu\rangle$ and corresponding eigenvalues $\Omega_\nu(\{0\})$ of the cluster Hamiltonian in (13) with on-site energies $\varepsilon_l = 0$. We present details of the evaluation of these states in an Appendix.

As a concrete numerical example, we choose a chemical potential of $\mu/U = 0.4$ which, for small J/U , places the system in the first Mott lobe with $\langle \hat{n} \rangle = 1$. The eigenvalues of the energy matrix are obtained by solving (28), whereas the eigenvalues of the stability matrix are obtained from (42). The four non-zero eigenvalues of these two matrices are shown in Fig. 4 as a function of J/U . We observe that one eigenvalue of the energy matrix associated with the eigenvector \mathbf{v}_1 increases from zero to positive values, and then passes through zero at the critical hopping $J_c/U = 0.04815$ which locates the MI-SF phase boundary for this value of μ/U . At this same hopping one finds that one of the eigenvalues of the stability matrix first attains a magnitude of one, consistent with the discussion following (52). Figure 5 displays the variation of the eigenvector components of these two specific eigenstates, namely, the eigenvector \mathbf{v}_1 of (28) and the eigenvector \mathbf{z}_1 of (42). Both of these eigenvectors have the form $(\psi_A, \psi_A, \psi_A, \psi_A, \psi_B, \psi_B)^T$. One sees that these two eigenvectors are the same ($\mathbf{z}_1 = \mathbf{v}_1$) at the MI-SF phase boundary and that (53) is indeed satisfied.

Although we allowed for a six-component order parameter in the above analysis, we find that the relevant eigenvectors \mathbf{v}_1 and \mathbf{z}_1 only have two independent components corresponding to the two inequivalent sites in the 3×2 cluster. One, ψ_A , is associated with the four corner sites and the other, ψ_B , is associated with the two edge sites. As can be seen in Fig. 5, these two values are almost equal for J/U close to the MI-SF transition. Even though the cluster does not mirror the symmetry of the square lattice, the violation of homogeneity is relatively weak. This behaviour persists into the SF phase. Fig. 6 shows that the self-consistently determined order parameters are close to each other over the range of hoppings indicated. The variation shown in Fig. 6 is consistent with the mean-field prediction in (32), as is the ratio of the two components. Also shown in this figure is the grand potential $\Omega_0(\{\psi_\alpha\})$ for the order parameter $\psi = (\psi_A, \psi_A, \psi_A, \psi_A, \psi_B, \psi_B)^T$ as a function of ψ_A , where the ratio ψ_B/ψ_A is fixed and taken from Fig. 5 at $J/U = 0.04815$. In the SF phase the grand potential shows minima at points which are very close to the order parameters determined self-consistently according to (15). Thus, near the phase boundary, the grand potential is indeed given to a good approximation by the Landau expansion in (31).

In view of the fact that the relevant eigenvector \mathbf{v}_1 only has two independent order parameter components, namely ψ_A and ψ_B , it is of interest to see to what extent the calculations can be simplified by assuming an order parameter having the form $\psi = (\psi_A, \psi_A, \psi_A, \psi_A, \psi_B, \psi_B)^T$. With this assumed form, the eigenvalue problem in (28) reduces to

$$\underline{W}^{\text{red}} \psi^{\text{red}} \equiv \begin{pmatrix} W_{AA} & W_{AB} \\ W_{BA} & W_{BB} \end{pmatrix} \begin{pmatrix} \psi_A \\ \psi_B \end{pmatrix} = \omega \begin{pmatrix} N_A & 0 \\ 0 & N_B \end{pmatrix} \begin{pmatrix} \psi_A \\ \psi_B \end{pmatrix}, \quad (56)$$

where N_A and N_B are the number of occurrences of ψ_A and ψ_B , respectively, in the order parameter vector. For this specific example, $N_A = 4$ and $N_B = 2$. The reduced matrix elements in (56) are defined as

$$W_{AA} = \sum_{i \in A} \sum_{j \in A} W_{ij}, \quad W_{AB} = \sum_{i \in A} \sum_{j \in B} W_{ij}, \quad W_{BA} = \sum_{i \in B} \sum_{j \in A} W_{ij}, \quad W_{BB} = \sum_{i \in B} \sum_{j \in B} W_{ij}. \quad (57)$$

By the same token, the expansion of the grand potential in (26) is given by

$$\Omega_0(\psi_A, \psi_B) = \Omega_0(0, 0) + \begin{pmatrix} \psi_A & \psi_B \end{pmatrix} \begin{pmatrix} W_{AA} & W_{AB} \\ W_{BA} & W_{BB} \end{pmatrix} \begin{pmatrix} \psi_A \\ \psi_B \end{pmatrix}. \quad (58)$$

We note that the eigenvalues of the matrix $\underline{W}^{\text{red}}$ appearing in this expression do *not* in general yield the desired \underline{W} eigenvalues which must be obtained from the generalized eigenvalue problem in (56).

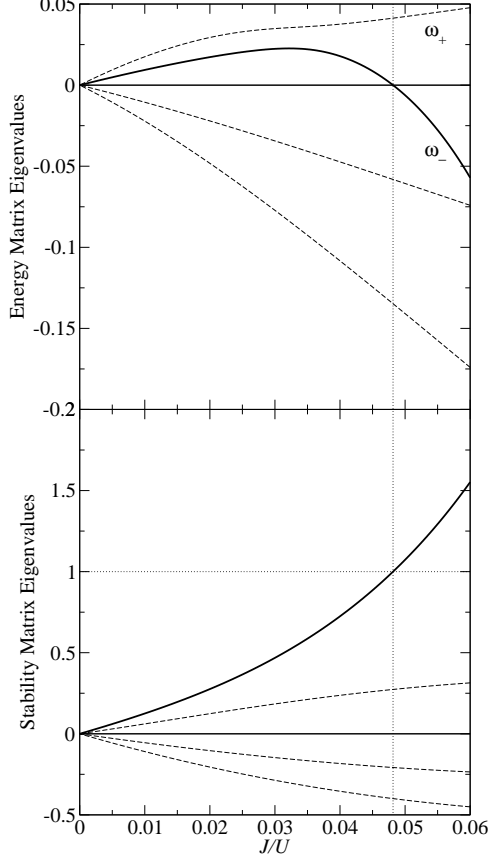


FIG. 4: The non-zero eigenvalues of the energy (top panel, in units of U) and stability (bottom panel) matrices for a homogeneous two-dimensional square lattice using a 3×2 cluster vs. J/U . The chemical potential is $\mu/U = 0.4$. One eigenvalue of the energy matrix crosses zero at $J/U = 0.04815$, the same position at which one eigenvalue of the stability matrix first attains a magnitude of one (the solid black curve in each figure). The superfluid phase is the $T = 0$ ground state for $J/U > 0.04815$.

Performing the sums in (57), we obtain the explicit expressions

$$W_{AA} = z_A N_A J + z_A^2 J^2 \sum_{\nu \neq 0} \frac{|\langle \nu | \sum_{i \in A} (\hat{a}_i^\dagger + \hat{a}_i) | 0 \rangle|^2}{\Omega_0(\{0\}) - \Omega_\nu(\{0\})}, \quad (59)$$

$$W_{BB} = z_B N_B J + z_B^2 J^2 \sum_{\nu \neq 0} \frac{|\langle \nu | \sum_{i \in B} (\hat{b}_i^\dagger + \hat{b}_i) | 0 \rangle|^2}{\Omega_0(\{0\}) - \Omega_\nu(\{0\})}, \quad (60)$$

and

$$W_{AB} = z_A z_B J^2 \sum_{\nu \neq 0} \frac{\langle 0 | \sum_{i \in A} (\hat{a}_i^\dagger + \hat{a}_i) | \nu \rangle \langle \nu | \sum_{j \in B} (\hat{b}_j^\dagger + \hat{b}_j) | 0 \rangle}{\Omega_0(\{0\}) - \Omega_\nu(\{0\})}. \quad (61)$$

Here we have introduced the notation \hat{a}_i (\hat{b}_i) for the site operators of the A (B) sites and define the connectivity number z_A (z_B). For the specific example of the 3×2 cluster, we have $z_A = 2$ and $z_B = 1$. The element W_{BA} is

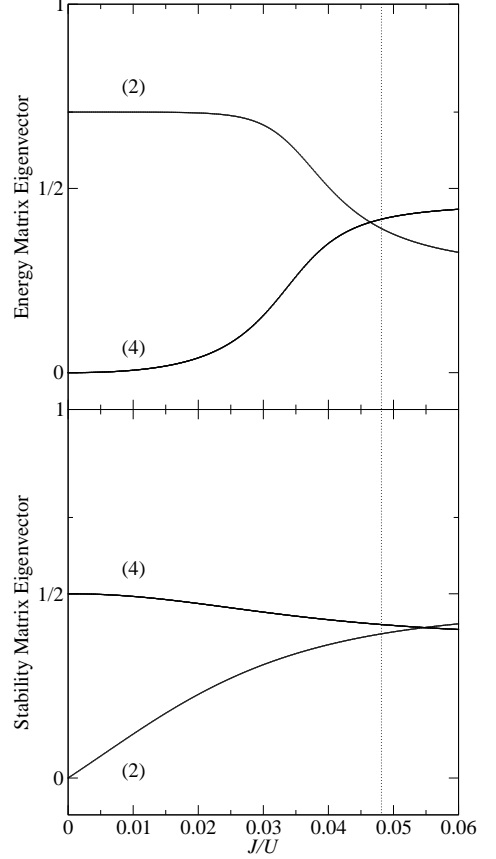


FIG. 5: The normalized eigenvector components corresponding to the energy (top) and stability (bottom) eigenvalues shown by the solid black curves in Fig. 4 vs. J/U . The bracketed numbers give the number of components having the indicated values, and correspond to the corner sites (multiplicity 4) and edge sites (multiplicity 2) of the 3×2 cluster. Note that at the transition these eigenvectors are the same, as required by (53).

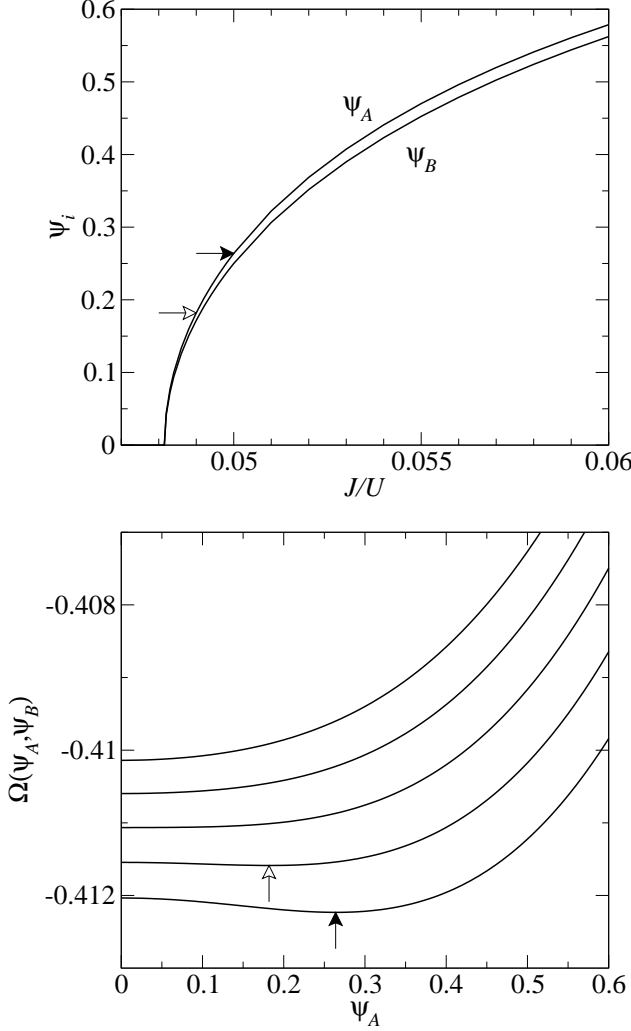


FIG. 6: The upper figure shows the self-consistently determined order parameters corresponding to the corner (ψ_A) and edge (ψ_B) sites of the 3×2 cluster as a function of J/U . The arrows indicate the values of ψ_A at $J/U = 0.049$ and 0.05 . The lower figure shows the grand potential as a function of ψ_A for the fixed ratio $\psi_B/\psi_A = 0.9396$ found at the phase boundary at $J/U = 0.04815$. The curves from top to bottom are for values of J/U from 0.046 to 0.050 in steps of 0.001 . In the SF phase, the grand potential shows minima at positions which are very close to the values of ψ_A found from the self-consistent calculations (indicated by the arrows). These results were obtained for $\mu/U = 0.4$.

obtained from W_{AB} by interchanging A and B . Since the matrix elements can be chosen to be real, we in fact have $W_{BA} = W_{AB}$.

The assumption of a two-component order parameter can also be used at the very beginning of this analysis to simplify the mean-field perturbation in (11). One finds for the example being considered that

$$\hat{\mathcal{V}}_{3 \times 2}^{MF} = -z_A J \psi_A \sum_{i \in A} (\hat{a}_i^\dagger + \hat{a}_i) - z_B J \psi_B \sum_{i \in B} (\hat{b}_i^\dagger + \hat{b}_i) + N_A z_A J \psi_A^2 + N_B z_B J \psi_B^2. \quad (62)$$

A perturbative treatment of this mean-field perturbation will of course yield precisely the grand potential in (58). However, the direct calculation of (58) does not by itself reveal the correct eigenvalue equation (56) required in the determination of the \underline{W} eigenvalues.

The eigenvalues of the energy matrix in (56) are

$$\omega_\pm = \frac{1}{2}(\bar{W}_{AA} + \bar{W}_{BB}) \pm \sqrt{\left(\frac{\bar{W}_{AA} - \bar{W}_{BB}}{2}\right)^2 + \bar{W}_{AB}^2}, \quad (63)$$

where $\bar{W}_{PQ} = W_{PQ}/\sqrt{N_P N_Q}$. In the limit $J \rightarrow 0$, we find that $\omega_+ \simeq z_A J$ and $\omega_- \simeq z_B J$. Thus, when symmetry is used to reduce the order parameter to the two components ψ_A and ψ_B , we see that the two energy matrix eigenvalues provided by the reduction increase linearly with J and are positive. In fact, these two eigenvalues correspond to the two eigenvalues in Fig. 6 which increase positively from zero. We thus see that the reduced grand potential has a local minimum for small J . This behaviour should be contrasted with the result obtained using the full six-component order parameter for which negative eigenvalues of the energy matrix are found even in the limit of small J (see Fig. 6).

To determine the MI-SF phase boundary with increasing J we must find a zero crossing of one of the ω_\pm eigenvalues. Since $\omega_+ > \omega_-$ for all values of J , the eigenvalue which first goes to zero is ω_- . Thus the location of the phase boundary is given by the condition

$$\frac{1}{2}(\bar{W}_{AA} + \bar{W}_{BB}) - \sqrt{\left(\frac{\bar{W}_{AA} - \bar{W}_{BB}}{2}\right)^2 + \bar{W}_{AB}^2} = 0, \quad (64)$$

which is equivalent to

$$W_{AA}W_{BB} = W_{AB}^2. \quad (65)$$

We will use this equation in the following section to map out the MI-SF phase boundary for the two-dimensional square lattice. We note that the N_A and N_B factors have dropped out in (65) as they must since they play no role in (56) when $\omega = 0$. In other words, it is sufficient to look for the zero eigenvalue of $\underline{W}^{\text{red}}$ in the determination of the phase boundary. Also, the ratio of the order parameter components just as one enters the SF region will be given by

$$\frac{\psi_B}{\psi_A} = \sqrt{\frac{W_{BB}}{W_{AA}}}. \quad (66)$$

In light of the very similar numerical values of ψ_A and ψ_B shown above, it is reasonable to try one final simplification, namely, enforcing the identity $\psi_A = \psi_B$. When such an order parameter vector is used, the energy and stability matrices reduce to scalars and one recovers a single order-parameter theory. The critical hopping parameter obtained in this case for $\mu/U = 0.4$ is $J_c/U = 0.04816$, as compared to $J_c/U = 0.04815$ obtained by allowing ψ_A and ψ_B to be different. Clearly, the inequivalence of different boundary sites in the MSMFT does not in itself adversely affect the prediction of the location of the MI-SF phase boundary for a homogeneous lattice.

III. APPLICATION TO HOMOGENEOUS LATTICES IN 1, 2, AND 3 DIMENSIONS

In this section we present our results for bosons on homogeneous lattices in d dimensions, focussing on the linear chain, square, and simple cubic lattices. We discuss the phase diagrams that are predicted by MSMFT, and the spatial correlations that are incorporated into ground-state wave functions found using this approach.

First, we consider the phase diagram of the linear chain in the region of the first Mott lobe ($0 < \mu/U < 1$). The relevant MSMFT data is shown in Fig. 7. “Exact” numerical results, found from a DMRG study [6], are also shown for comparison. The SDMFT result is seen to be far from the exact phase boundary, a result well known in the literature [6, 32]. In Fig. 7 we also show the results from the application of MSMFT for L -mers of size $L = 2, 4, 8$. One can see that as L increases the extent of the Mott lobe approaches the DMRG results. Therefore, in one dimension we find that there is a systematic improvement in identifying the phase boundary upon going from SDMFT to MSMFT. However, the predicted phase boundaries are still not close to the exact results and lack the cusp-like feature at the tip of the lobe. Further improvements could be achieved by increasing L but the progression in Fig. 7 suggests that going to $L = 16$ would provide only a modest improvement. This value of L is already beyond our numerical capabilities.

Also shown in Fig. 7 are results obtained from an exact diagonalization of the full Hamiltonian in (1) for a finite linear chain with periodic boundary conditions. Since the Hamiltonian commutes with the total number operator, one can determine the N -domains in the μ/U - J/U plane where the ground state of \hat{K} has a total of N particles. For chains of length N_s , the first Mott lobe must be found in the region where $N = N_s$, at least in the limit $N_s \rightarrow \infty$. The boundaries of the $N = N_s$ region are shown in Fig. 7 for chains of length $N_s = 5$ and 10 . It is clear from the figure that the $N = N_s$ domain bounds the exact Mott lobe with increasing accuracy with increasing N_s . However, exact diagonalizations for much longer chains would be necessary to accurately represent the tip of the Mott lobe.

Our results in two dimensions are shown in Fig. 8. In the MSMFT calculations we have used clusters of sizes 2×2 and 3×3 ; the “exact” results are taken from the Monte Carlo study of Ref. [9]. As in the previous figure we also show the boundaries of the N -domain ($N = 9$ in this case) for the exact solution of the full Hamiltonian of a 3×3 cluster with periodic boundary conditions. To perform the calculations for the largest cluster it was necessary to take

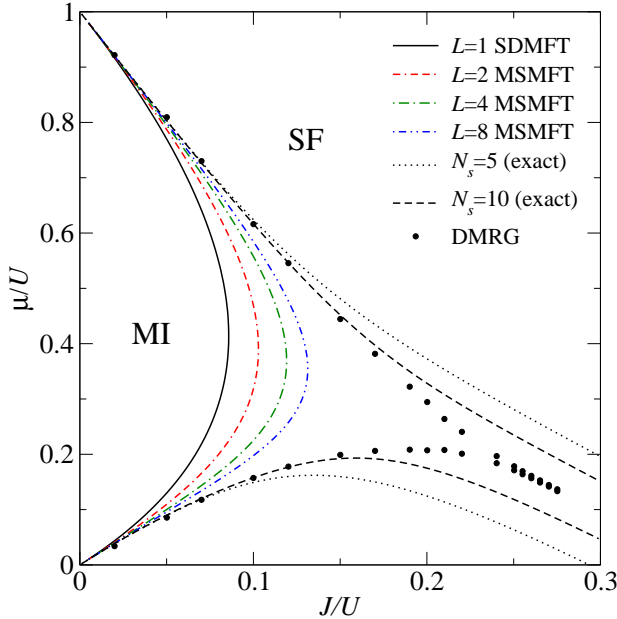


FIG. 7: [Colour online] The MI-SF phase boundaries for a linear chain predicted by MSMFT, compared to the DMRG results of [6] shown as circles. The phase boundary systematically approaches the exact result with increasing length L of the cluster: $L = 2$ (dash-dash-dot red line), $L = 4$ (dot-dash green line), $L = 8$ (dot-dot-dash blue line). Also shown are the boundaries of the N -domain where the ground state of the full Hamiltonian for a finite chain of length N_s has $N = N_s$ particles.

advantage of the symmetry of the cluster; some details of the method used are given in the Appendix. Similar results are shown in Fig. 9 for three dimensions, where we have performed calculations for $2 \times 2 \times 1$ and a $2 \times 2 \times 2$ clusters. One sees a progressive improvement of the phase boundary with increasing cluster size, as in the case of the linear chain, with the phase boundary approaching the exact (MC) results [8]. The best agreement is obtained in three dimensions as one might expect on the basis of the validity of mean field theory when the upper critical dimension is approached.

For the 3×3 cluster in Fig. 2(b), the A and B sites are inequivalent and as a result, the order parameters ψ_A and ψ_B as one enters the SF phase will be different. We find, however, that the ratio given in (66) deviates from unity by no more than a few percent. It is therefore of interest to see the effect of enforcing the equality of ψ_A and ψ_B in the MSMFT calculations. (Note that this does not reduce MSMFT to SDMFT since one must still determine the eigenstates of \hat{K}_L^0 for the whole cluster.) We find that the phase boundaries shown in the two-dimensional phase diagram are virtually unchanged when this constraint on the order parameters is imposed. Thus the calculations for homogeneous lattices can be simplified by assuming that the order parameters of all the boundary sites of the cluster are the same.

With several sites in the cluster, one can also consider *spatial correlations* between the various sites. As mentioned in the introduction, this is one of the main advantages of using a MSMFT. The correlations we consider are those exhibited by the function

$$C_{ij} = \langle \hat{\phi}_i^\dagger \hat{\phi}_j \rangle, \quad (67)$$

where

$$\hat{\phi}_i = \hat{a}_i - \langle \hat{a}_i \rangle. \quad (68)$$

In the MI phase, C_{ij} reduces to the single-particle density matrix while in the SF phase it is the contribution to the density matrix from the noncondensed component.

We first consider our results for the linear chain, specifically along the $\mu/U = 0.4$ line in the phase diagram of Fig. 7. For a given L -mer, we calculate $C_{i,i+l}$ for all possible values of i and l consistent with the size of the L -mer. In the MI phase we find that $C_{i,i+l}$ has a rather weak dependence on the position i within the cluster despite the fact that the states of the cluster are calculated with open-chain boundary conditions. For this reason we plot only $\bar{C}_l(L)$, the average of $C_{i,i+l}$ over i . This quantity is shown in Fig. 10 for $L = 7$ for l between 0 and 6 and for values of J/U that span the phase boundary. Since this log-linear plot reveals a dependence on l which deviates weakly from a pure

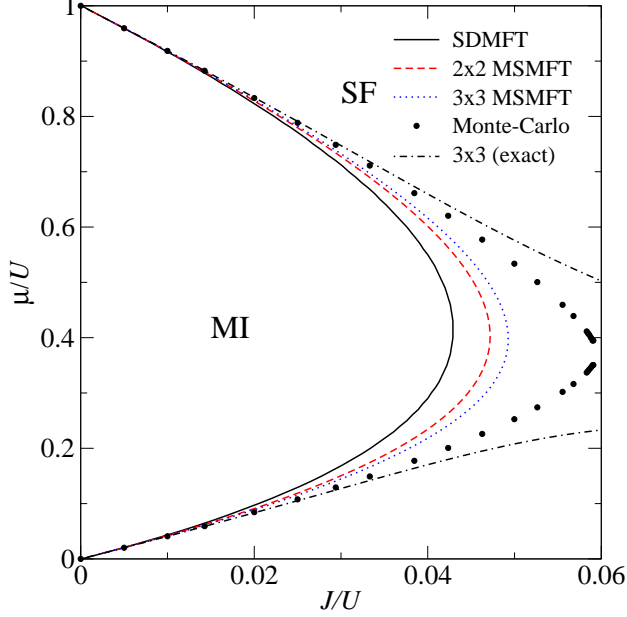


FIG. 8: [Colour online] The MI-SF phase boundaries for a two-dimensional square lattice, as calculated using SDMFT (solid black line) and MSMFT (2×2 , dashed red line; 3×3 (dotted blue line). The MC data (solid black circles) are taken from Ref. [9]. Also shown (dot-dash black line) is the N -domain ($N = 9$) for the 3×3 cluster determined by calculating the ground state of the full (non-MFT) Hamiltonian with periodic boundary conditions.

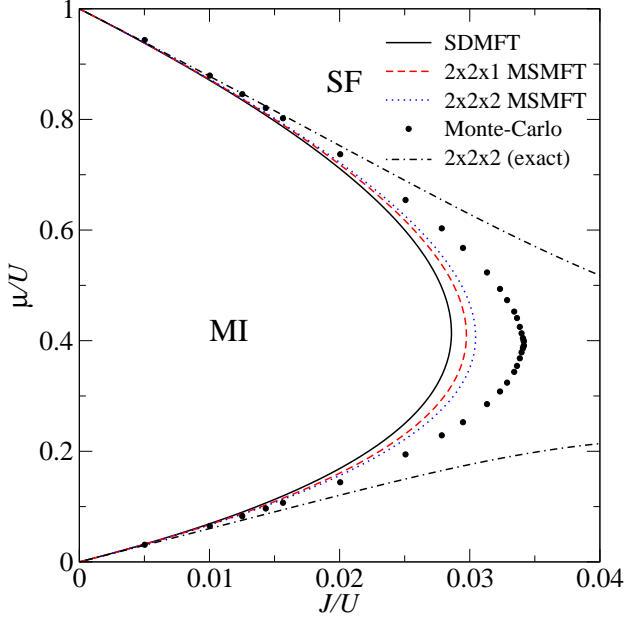


FIG. 9: [Colour online] The MI-SF phase boundaries for a three-dimensional cubic lattice, as calculated using SDMFT (solid black line) and MSMFT ($2 \times 2 \times 1$, dashed red line; $2 \times 2 \times 2$, dotted blue line). The MC data (solid black circles) taken from Ref. [8].

exponential, we have fit this data to the form

$$\bar{C}_l(L) \sim \frac{e^{-l/\xi}}{(l_0 + l)^\eta}, \quad (69)$$

where the fit parameters l_0 , ξ and η are in general functions of L [42]. We emphasize that this form of fitting function is chosen simply because it describes the *short-range* behaviour of the correlation function with reasonable accuracy.

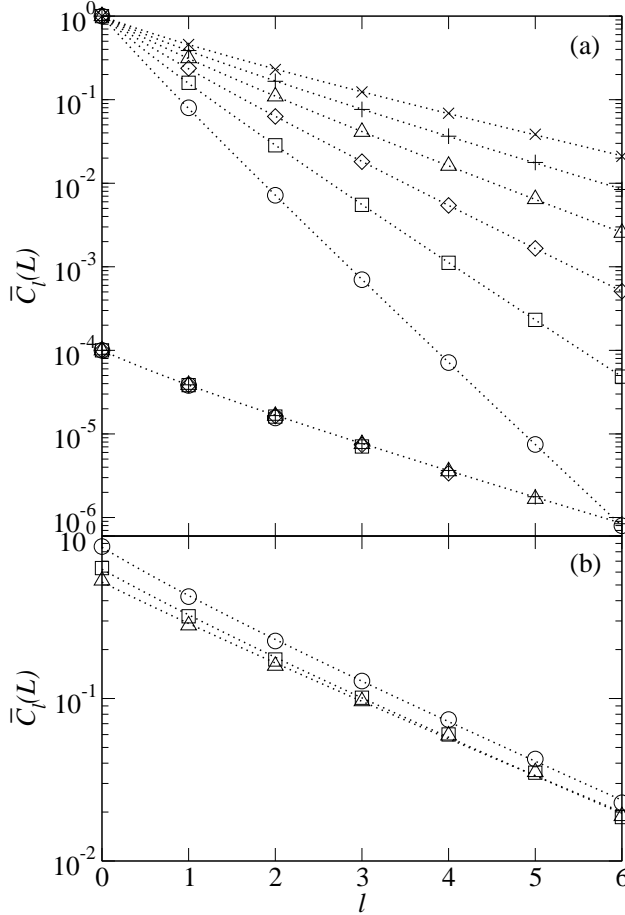


FIG. 10: The average correlation function of the linear chain within MSMFT versus the intersite spacing. Panel (a) shows results for $L = 7$ in the MI phase: the six curves starting from 1 at $n = 0$ correspond, from bottom to top, to $J/U = 0.02, 0.04, 0.06, 0.08, 0.10$ and 0.12 . The points are the calculated values of $\bar{C}_l(L)$ and the dashed curves are plots of the fitting function (69). The lowest curve in (a) shows results for $J/U = 0.10$ for $L = 3, 4, 5, 6$ and 7 , all plotted on top of each other. This curve has been displaced from the others for clarity by multiplying the data by 10^{-4} . Panel (b) shows results for $L = 7$ in the SF phase: from top to bottom, $J/U = 0.14, 0.17$, and 0.20 .

In the limit $L \rightarrow \infty$, one in principle would be able to determine the asymptotic behaviour of the correlation function which for large l should behave as

$$\bar{C}_l(\infty) \sim \frac{e^{-l/\xi_\infty}}{l^{\eta_\infty}}. \quad (70)$$

At the phase boundary, one expects ξ_∞ to diverge [6], resulting in an algebraic decay of the correlation function. However, the finite size of the L -mers considered in our calculations precludes extracting useful information about this asymptotic behaviour.

We also observe that in the MI phase the values of $\bar{C}_l(L)$ for a fixed l depend weakly on L . This is confirmed by the lowest curve in Fig. 10(a) for $J/U = 0.1$ where we plot all the available data for $\bar{C}_l(L)$ for $L = 3, \dots, 8$. This shows that the short-range behaviour of the $\bar{C}_l(L)$ correlation function is not affected significantly by increasing the cluster size. The results in the SF phase are shown for $L = 7$ in Fig. 10(b). The behaviour shown here is qualitatively different from the MI phase.

In Fig. 11 we show the correlation length $\xi(L)$ obtained by fits of the data to (69) as a function of J/U . In the MI phase there is a monotonic increase of ξ with J/U , reaching a peak (or cusp) at the phase boundary between the MI and SF phases, the position of which of course depends on L . As stated earlier, the variation of ξ with L at a fixed value of J/U is relatively weak in the MI phase; part of this variation is simply a result of fitting data over an increasingly larger range of l . However, the L -dependence of $\xi(L)$ is much stronger in the SF phase. The distinct behaviour of $\xi(L)$ between the MI and SF phases persists for all values of μ/U . As for the other fitting parameters, we

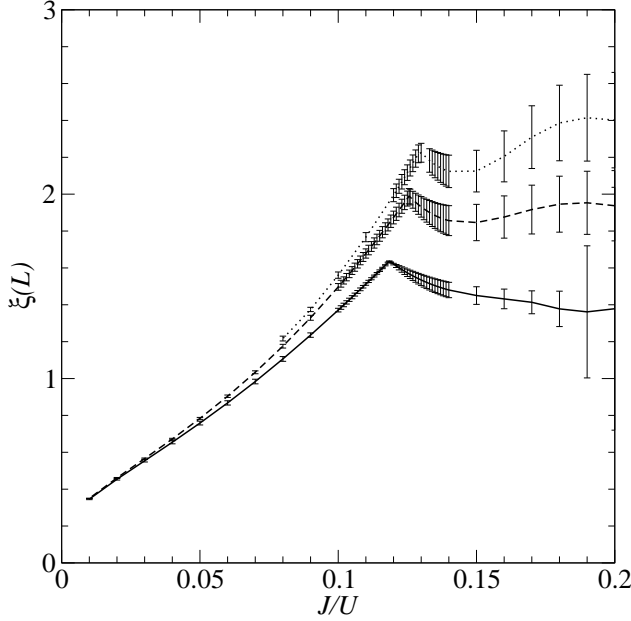


FIG. 11: The correlation length $\xi(L)$ vs. J/U for the linear chain of length $L = 4, 6$ and 8 (bottom to top). The results were obtained by fitting the data to (69); the vertical bars indicate the estimated error.

find that $l_0 \simeq 1$ in the MI phase, reflecting the fact that $\bar{C}_{l=0}(L) \simeq 1$; l_0 then increases slightly as $\bar{C}_{l=0}(L)$ decreases in the SF phase. Finally, we find that $\eta(L)$ is close to 0.4 for most of the data considered.

Rather similar behaviour is found for the two-dimensional 3×3 cluster in Fig. 2(b) in the MI phase. For this cluster there are five distinct intersite separations r_{ij} , namely $1, \sqrt{2}, 2, \sqrt{5}$, and $2\sqrt{2}$ in units of the lattice constant. Due to the finite size of the cluster, there are pairs of sites, such as the nearest-neighbour AB and BC sites, for which the correlations are not equivalent. However, the differences are found to be small and we therefore average the correlations over all pairs of sites which, by symmetry, would be equivalent in the infinite lattice. These averaged values are plotted in Fig. 12.

The data in Fig. 12 were fit to a function having the following form

$$\bar{C}_{ij} = e^{-r_{ij}/\xi} (a + b(1 - \delta_{ij}) \cos 4\theta_{ij}), \quad (71)$$

where ξ is again the correlation length, and the parameters a and b are introduced to capture the anisotropy of the lattice correlation function. The variable θ_{ij} is the angle that the vector \mathbf{r}_{ij} makes with the x -axis. The values of \bar{C}_{ij} as determined by (71) are also plotted in Fig. 12 for the optimal values of the fitting parameters. These values are joined by the dotted lines to provide a guide to the eye. It can be seen that the data points lie quite close to these lines for all J/U , indicating that the assumed form of the angular dependence does a reasonable job of representing the data. The correlation length ξ is plotted in Fig. 13 as a function of J/U . The increasing trend is similar to that found for the linear chain, but the 2D correlation length is significantly smaller than in 1D. We emphasize again that the correlation length we have extracted represents the short-range behaviour of the correlation function. One would need the long-range behaviour in order to determine the critical behaviour of the correlation length at the MI-SF phase boundary.

Finally, we consider the occupation number distribution for a particular site in the L -mer in the MI phase. The probability of finding the configuration $|\{n_l\}\rangle$ in $|0\rangle$, the ground state of \mathcal{K}_L^0 , is $|\langle\{n_l\}|0\rangle|^2$. Thus the occupation number distribution for, say site 1, is

$$P(n_1) = \sum_{n_2, \dots, n_l} |\langle\{n_l\}|0\rangle|^2. \quad (72)$$

Near the tip of the first Mott lobe of the 3×3 L -mer of the 2D square lattice ($\mu/U = 0.4$, $J/U = 0.049$) we find $P(0) = 0.022$, $P(1) = 0.955$ and $P(2) = 0.023$ for the central site of the 3×3 L -mer. Even though the average occupancy of the sites within the L -mer is exactly $n = 1$ in the MI phase, the occupancy of a given site does fluctuate about its average value; the probability of finding 0 or 2 particles on this site is roughly 2%.

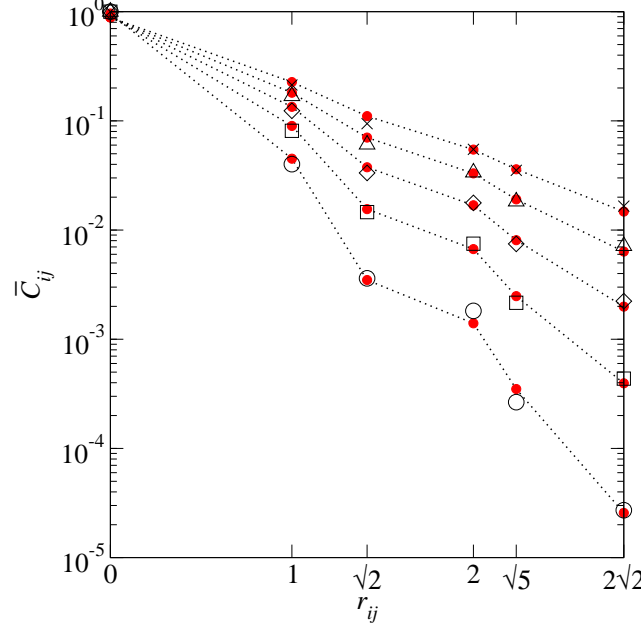


FIG. 12: [Colour online] The variation of the averaged pair correlations with separation in units of the lattice constant for the two-dimensional 3×3 cluster. The points are the result of the MSMFT calculation for $\mu/U = 0.4$ and for $J/U = 0.01$ (circle), 0.02 (square), 0.03 (diamond), 0.04 (triangle) and 0.049 (cross). The values of \bar{C}_{ij} as obtained from the fitting function in (71) are also plotted as solid points (red) which are joined by dotted lines as a guide to the eye. The MI-SF transition for this value of μ/U occurs close to $J/U = 0.0492$.

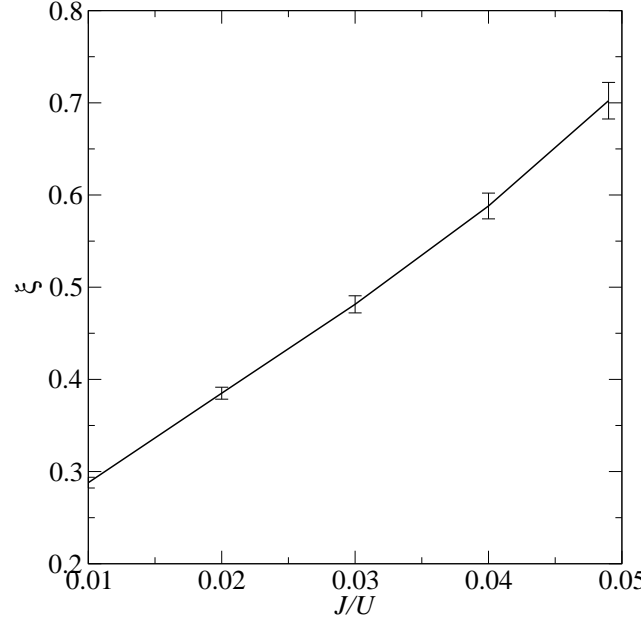


FIG. 13: The dependence of the correlation length, ξ (in units of the lattice constant), on J/U for the two-dimensional square lattice using a 3×3 cluster. The results were obtained by fitting the data in Fig. 12 to (71).

IV. APPLICATION TO SUPERLATTICES

A. The Dimer Chain

We now turn to an analysis of a simple superlattice consisting of a one-dimensional chain in which the on-site energies alternate in an $\dots \varepsilon_A \varepsilon_B \varepsilon_A \varepsilon_B \dots$ fashion. Figure 14 shows a portion of such a lattice, with a pair of AB sites being referred to as a *dimer*. The BH Hamiltonian for this system can then be expressed as

$$\hat{\mathcal{K}} = \frac{\Delta}{2} \sum_j (\hat{n}_j^B - \hat{n}_j^A) - \mu \sum_j (\hat{n}_j^A + \hat{n}_j^B) + \frac{1}{2} \sum_j (U_A \hat{n}_j^A (\hat{n}_j^A - 1) + U_B \hat{n}_j^B (\hat{n}_j^B - 1)) \\ - J_1 \sum_j (\hat{a}_j^\dagger \hat{b}_j + \hat{b}_j^\dagger \hat{a}_j) - J_2 \sum_j (\hat{a}_{j+1}^\dagger \hat{b}_j + \hat{b}_j^\dagger \hat{a}_{j+1}), \quad (73)$$

where the index j labels the j th dimer within the lattice. Here, we have introduced the site operators $\hat{a}_j(\hat{a}_j^\dagger)$ and

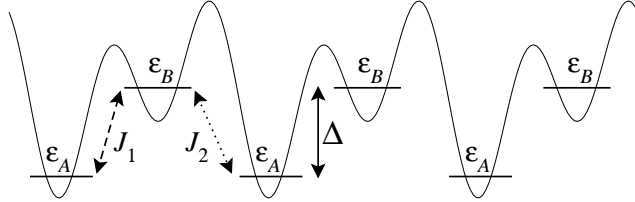


FIG. 14: Schematic of a general dimer superlattice with alternating site energies ε_A and ε_B . The level separation is Δ . The different barrier heights along the chain lead to different intra-dimer (J_1) and inter-dimer (J_2) tunnelling energies.

$\hat{b}_j(\hat{b}_j^\dagger)$ for the A and B sites, respectively, in the j th dimer, and the number operators $\hat{n}_j^A = \hat{a}_j^\dagger \hat{a}_j$ and $\hat{n}_j^B = \hat{b}_j^\dagger \hat{b}_j$. With $\varepsilon_A = -\Delta/2$ and $\varepsilon_B = \Delta/2$, the level separation within a dimer is Δ . We have also allowed for different interaction parameters U_A and U_B for the two kinds of sites and for different intra-dimer (J_1) and inter-dimer (J_2) hopping (tunnelling) energies. For the optical lattice potential illustrated in Fig. 14, the asymmetric barrier heights lead to $J_1 > J_2$. In the following, we consider the optical lattice shown in Fig. 15 which has inversion symmetry and symmetric barrier heights. In this case, $J_1 = J_2 = J$. For simplicity, we also assume $U_A = U_B = U$. This particular model was previously studied in [7] and [22].

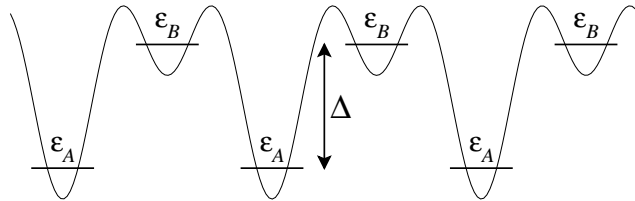


FIG. 15: A portion of the dimer superlattice used in the analysis of the MI-SF transition. The inversion symmetry about each lattice site results in equal intra- and inter-dimer tunnelling energies J .

To implement the MSMFT, we partition the lattice into clusters containing N_d dimers, thus defining L -mers of size $L = 2N_d$. Each L -mer begins with an A site and ends with a B site, and the different L -mers are decoupled by introducing the order parameters ψ_A and ψ_B . Following the procedure given in § II B, we obtain the mean-field decoupled L -mer Hamiltonian

$$\hat{\mathcal{K}}^{MF} = \hat{\mathcal{K}}_L^0 + \hat{\mathcal{V}}_L^{MF}, \quad (74)$$

where

$$\hat{\mathcal{K}}_L^0 = \sum_{j=1}^{N_d} \left[\left(-\frac{\Delta}{2} - \mu \right) \hat{n}_j^A + \left(\frac{\Delta}{2} - \mu \right) \hat{n}_j^B + \frac{U}{2} \left(\hat{n}_j^A (\hat{n}_j^A - 1) + \hat{n}_j^B (\hat{n}_j^B - 1) \right) \right] \\ - J \sum_{j=1}^{N_d} (\hat{a}_j^\dagger \hat{b}_j + \hat{b}_j^\dagger \hat{a}_j) - J \sum_{j=1}^{N_d-1} (\hat{a}_{j+1}^\dagger \hat{b}_j + \hat{b}_j^\dagger \hat{a}_{j+1}) \quad (75)$$

is the Hamiltonian of an open-ended dimer chain of length $L = 2N_d$, and

$$\hat{\mathcal{V}}_L^{MF} = -J\psi_B (\hat{a}_1^\dagger + \hat{a}_1) - J\psi_A (\hat{b}_{N_d}^\dagger + \hat{b}_{N_d}) + 2J\psi_A\psi_B \quad (76)$$

is the mean-field coupling.

To determine the MI-SF phase boundary we use the energy criterion based on the eigenvalues of the energy matrix \underline{W} . For this example of a two-component order parameter, the expansion of the grand potential has the form given in (58) with the matrix elements

$$W_{AA} = J^2 \sum_{\nu \neq 0} \frac{|\langle \nu | \hat{b}_{N_d}^\dagger + \hat{b}_{N_d} | 0 \rangle|^2}{\Omega_0(\{0\}) - \Omega_\nu(\{0\})}, \quad (77)$$

$$W_{BB} = J^2 \sum_{\nu \neq 0} \frac{|\langle \nu | \hat{a}_1^\dagger + \hat{a}_1 | 0 \rangle|^2}{\Omega_0(\{0\}) - \Omega_\nu(\{0\})}, \quad (78)$$

$$W_{AB} = J + J^2 \sum_{\nu \neq 0} \frac{\langle 0 | \hat{b}_{N_d}^\dagger + \hat{b}_{N_d} | \nu \rangle \langle \nu | \hat{a}_1^\dagger + \hat{a}_1 | 0 \rangle}{\Omega_0(\{0\}) - \Omega_\nu(\{0\})}, \quad (79)$$

and $W_{BA} = W_{AB}$. The \underline{W} eigenvalues in this case are given by

$$\omega_{\pm} = \frac{1}{2}(W_{AA} + W_{BB}) \pm \sqrt{\left(\frac{W_{AA} - W_{BB}}{2} \right)^2 + W_{AB}^2}. \quad (80)$$

Since W_{AA} and W_{BB} are negative definite, we see that $\omega_- < 0$. On the other hand, since $W_{AB} \simeq J$ for small J , while W_{AA} and W_{BB} are proportional to J^2 , we see that ω_+ remains positive with increasing J up to the point where

$$W_{AA}W_{BB} = W_{AB}^2, \quad (81)$$

when it goes to zero. This equation defines the phase boundary between the MI and the SF phases. We thus see that $\psi = \mathbf{0}$ is a saddle point of the grand potential in the MI phase and that this point turns into a local maximum when the SF phase is entered. The stationary point remains a saddle point in the SF phase.

1. Results for $N_d = 1$

In this subsection we present results for the case of an L -mer consisting of a single dimer, that is, $N_d = 1$. This case already exhibits all the general features of the phase diagram for a dimer chain. The results we obtain in the following subsection show quantitative improvements with increasing N_d but are qualitatively similar. The results we find for $N_d = 1$ are also similar to those found in an earlier investigation [22]. This latter work, however, is a SDMFT (even though different order parameters are introduced for the A and B sites) since the dimer Hamiltonian used in the perturbative analysis is the sum of independent site Hamiltonians. In contrast, ours is truly a MSMFT, even for $N_d = 1$, since it requires the determination of the eigenstates of the coupled dimer Hamiltonian in (75).

The phase diagram for the dimer chain is determined in the three-dimensional parameter space defined by the dimensionless variables $\tilde{\mu} = \mu/U$, $\tilde{J} = J/U$ and $\tilde{\Delta} = \Delta/U$. For given values of $\tilde{\mu}$ and $\tilde{\Delta}$, the system is in a MI phase for $\tilde{J} < \tilde{J}_{\text{cr}}(\tilde{\mu}, \tilde{\Delta})$. This function defines the phase boundary as a surface in the three-dimensional parameter space. As we shall see, this surface consists of sections, each of which terminates on the $\tilde{J} = 0$ plane and corresponds to distinct MI regions. In order to understand the underlying structure of the phase diagram, it is therefore useful to first consider the limiting case of $\tilde{J} = 0$ which defines the base of the Mott lobes. For $\tilde{J} = 0$ and $N_d = 1$, we have the dimensionless dimer Hamiltonian (we can dispense with the dimer index j in (75) since there is a single dimer in the L -mer)

$$\tilde{\mathcal{K}}_L^0(\tilde{J} = 0) = \left(-\frac{\tilde{\Delta}}{2} - \tilde{\mu} \right) \hat{n}_A + \left(\frac{\tilde{\Delta}}{2} - \tilde{\mu} \right) \hat{n}_B + \frac{1}{2} (\hat{n}_A (\hat{n}_A - 1) + \hat{n}_B (\hat{n}_B - 1)). \quad (82)$$

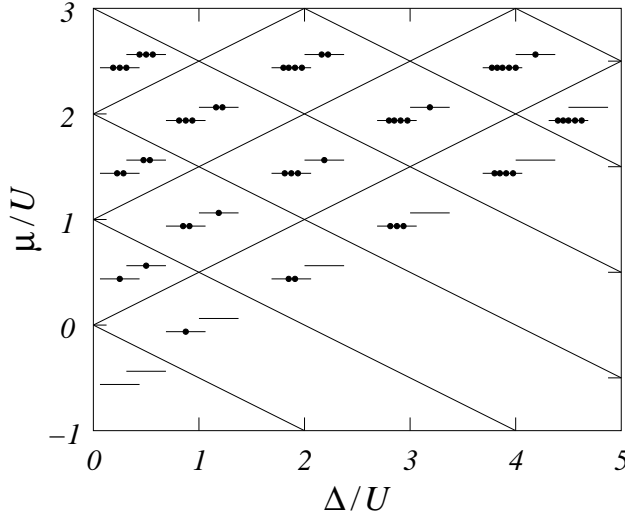


FIG. 16: The N -domains of a single-dimer L -mer at $\tilde{J} = 0$. The site occupations of the A (lower level) and B (upper level) sites is indicated by the number of black dots. As one crosses a downward (upward) sloping line with increasing μ/U , the occupation of the lower (upper) level increases by one. This figure applies to any number of dimers in the L -mer being considered.

The occupation number states $|n_A, n_B\rangle$ are eigenstates of this Hamiltonian with eigenvalues

$$\tilde{\kappa}_L^0 = \frac{1}{2} \left(n_A - \tilde{\mu}_A - \frac{1}{2} \right)^2 - \frac{1}{2} \left(\tilde{\mu}_A + \frac{1}{2} \right)^2 + \frac{1}{2} \left(n_B - \tilde{\mu}_B - \frac{1}{2} \right)^2 - \frac{1}{2} \left(\tilde{\mu}_B + \frac{1}{2} \right)^2, \quad (83)$$

where $\tilde{\mu}_A = \tilde{\mu} + \tilde{\Delta}/2$ and $\tilde{\mu}_B = \tilde{\mu} - \tilde{\Delta}/2$. The lowest energy is obtained by minimizing $\tilde{\kappa}_L^0$ with respect to n_A and n_B . Since n_A is an integer, the minimizing value of n_A is the integer closest to $\tilde{\mu}_A + 1/2$, that is, the integer ν_A when $\nu_A - 1 < \tilde{\mu}_A < \nu_A$. This condition defines a region in the $\tilde{\mu}$ - $\tilde{\Delta}$ plane where the number of atoms on the A site is ν_A . These regions are shown in Fig. 16 and are bounded by the lines $\tilde{\mu} = \nu_A - \tilde{\Delta}/2$ for $\nu_A = 0, 1, \dots$. A similar analysis determines ν_B , the minimizing value of n_B , and the regions where this value applies are bounded by the lines $\tilde{\mu} = \nu_B + \tilde{\Delta}/2$ with $\nu_B = 0, 1, \dots$. As shown in Fig. 16, the $\tilde{\mu}$ - $\tilde{\Delta}$ plane is thus divided into domains in which the number of particles in the dimer is $N = \nu_A + \nu_B$. These domains are the N -domains introduced earlier and define the base of the distinct MI regions. We observe that each of these regions has specific site occupations. For example, for $N = 2$, there is a region where the dimer configuration is given by $\nu_A = 1, \nu_B = 1$ and another with $\nu_A = 2, \nu_B = 0$. These two configurations are degenerate in energy at a single point in the $\tilde{\mu}$ - $\tilde{\Delta}$ plane. They are also degenerate with other configurations having a different value of N along the lines bounding the N -domains. With increasing \tilde{J} , the occupation number states are no longer eigenstates of the dimer Hamiltonian but within each Mott lobe the dimer configuration is predominantly that indicated in Fig. 16 at the base of the lobe.

In Fig. 17 we show a contour plot of the $\tilde{J}_{\text{cr}}(\tilde{\mu}, \tilde{\Delta})$ surface, below which the MI phase exists. The grey scale indicates the extent of the MI phase in the \tilde{J} direction which is perpendicular to the plane of the figure. In general, we see that the area enclosed by a given contour decreases as \tilde{J} increases, resulting in a dome-like structure of the MI-SF phase boundary. The $\tilde{J} = 0$ contour (black) corresponds to the lines in Fig. 16 and defines the base of each of the Mott lobes. Within each lobe the number of particles in the dimer, $\langle \hat{n}_A \rangle + \langle \hat{n}_B \rangle$, is equal to the integer N indicated by the configuration in Fig. 16. However, as we show in more detail later, the average site occupancies $\langle \hat{n}_A \rangle$ and $\langle \hat{n}_B \rangle$ are not constant throughout a given lobe.

Although Fig. 17 provides the overall structure of the phase diagram, it is useful to consider various two-dimensional cross-sections to visualize the MI and SF regions. A slice through Fig. 17 at a constant value of \tilde{J} gives one of the contours in the figure and reveals the Mott regions as islands in the $\tilde{\mu}$ - $\tilde{\Delta}$ plane surrounded by SF regions. Another possibility is a vertical slice through Fig. 17 at a fixed value of $\tilde{\Delta}$. In Fig. 18 we show such a slice at $\tilde{\Delta} = 0.75$. Together with Fig. 17 it is easy to visualize the variation of the MI regions with variations in $\tilde{\Delta}$.

Perhaps a more physical situation is that for a fixed optical lattice, hence fixed values of J and Δ , but with varying U which can be controlled experimentally by means of a Feshbach resonance. A cross-section at fixed J/Δ (i.e., $\tilde{J}/\tilde{\Delta}$) corresponds to a plane containing the $\tilde{\mu}$ axis and inclined at some angle with respect to the \tilde{J} and $\tilde{\Delta}$ axes. In Fig. 19 we show the intersection of such a plane with the Mott lobes in Fig. 17 for $J/\Delta = 0.05$. The superfluid phase is indicated by the ‘shaded’ region (the vertical black lines) surrounding the various MI phases that occur for different values of N . One can see that odd values of N , corresponding to a half-integral average number of particles per

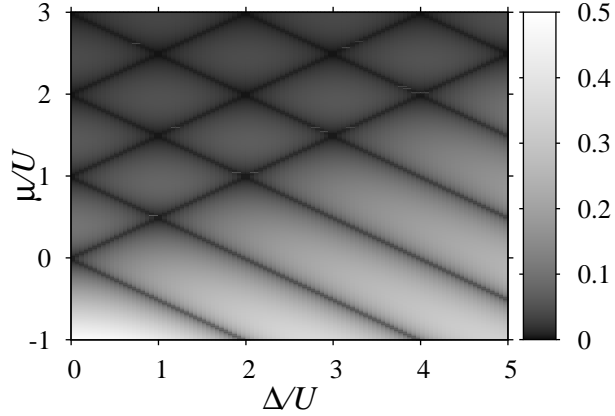


FIG. 17: The phase diagram of a dimer chain within the MSMFT using a cluster consisting of a single dimer. The grey scale indicates the value of $\tilde{J}_{\text{cr}}(\tilde{\mu}, \tilde{\Delta})$ at which the MI-SF phase boundary occurs. Each region bounded by a black contour ($\tilde{J} = 0$) corresponds to a different Mott lobe with an integer number of atoms N in the dimer.

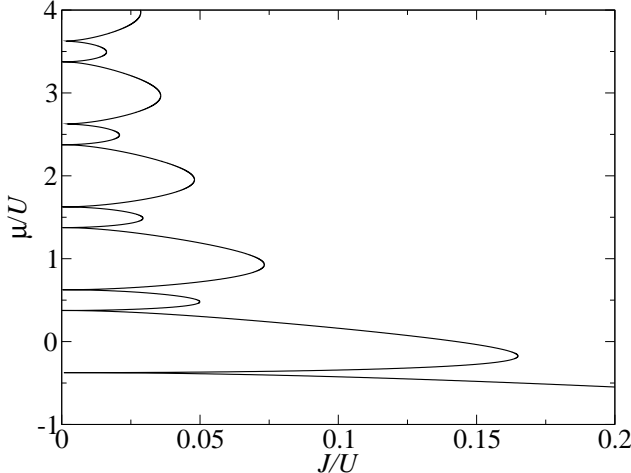


FIG. 18: A slice through the phase diagram in Fig. 17 at $\tilde{\Delta} = 0.75$. The average filling per site for each Mott lobe increases by $1/2$ with increasing μ/U , starting with $n = 0$ at the bottom of the figure. The system is a SF to the right of the phase boundary.

site, give rise to lobes which emerge at integral values of $\tilde{\mu}$. These lobes should not be confused with the so-called “loopholes” discussed in [15, 17] which arise for a different reason when more complex superlattice structures are considered.

Also shown in Fig. 19 are the various N -domains which are bounded by the solid curves. These domains evolve continuously from those shown in Fig. 16 as the $J/\Delta = 0$ plane is tilted into the $J/\Delta = 0.5$ plane. As one can see, the crossings of the domain boundaries in Fig. 16 become avoided crossings as a result of the finite value of J . These avoided crossings become more pronounced with increasing $\tilde{\Delta}$ since $\tilde{J} = 0.05\tilde{\Delta}$.

2. Results for $N_d > 1$

We next consider the effect of increasing the number of dimers in the L -mer to $N_d = 2$. The $\tilde{J} = 0$ phase diagram is the same as in Fig. 16 but the site occupancies shown should be understood to apply to both dimers so that the number of particles in each of the N -domains is actually doubled. The difference from $N_d = 1$ becomes apparent for

$\tilde{J} \neq 0$ and in Fig. 20 we show the phase diagram for $J/\Delta = 0.05$. This phase diagram is very similar to the $N_d = 1$ phase diagram in Fig. 19 apart from the appearance of a new Mott region for $N = 6$ corresponding to an average filling ($n = N/L$) of $n = 3/2$ particles per site. This simply reflects the fact that the Mott regions are stabilized with increasing L -mer size as found for the homogeneous systems discussed in §III. As N_d increases, $\tilde{J}_{\text{cr}}(\tilde{\mu}, \tilde{\Delta})$ increases and the Mott lobes in Fig. 17 extend to larger values of \tilde{J} . The intersection of the $J/\Delta = 0.05$ plane with the Mott lobes can thus include additional Mott regions as found in the present example.

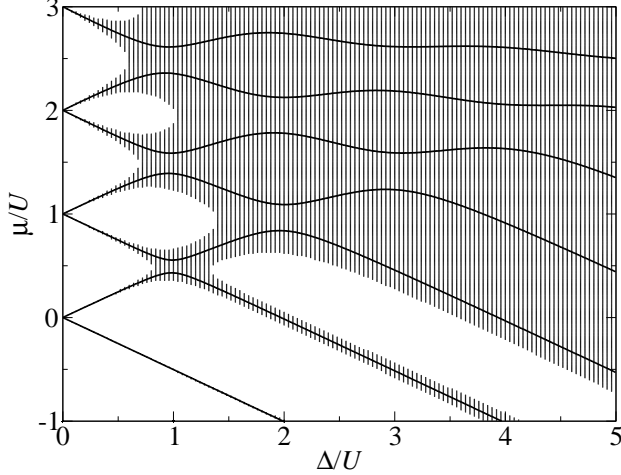


FIG. 19: The phase diagram of the dimer chain obtained for an L -mer consisting of a single dimer at $J/\Delta = 0.05$. The SF phase is indicated by the shaded region (the vertical black lines) which surround the various MI regions. The black lines are the boundaries of the N -domains within which Mott regions with N particles per dimer are located. As discussed in the text, the N -domains are the regions where the ground state of \hat{K}_L^0 contains N particles.

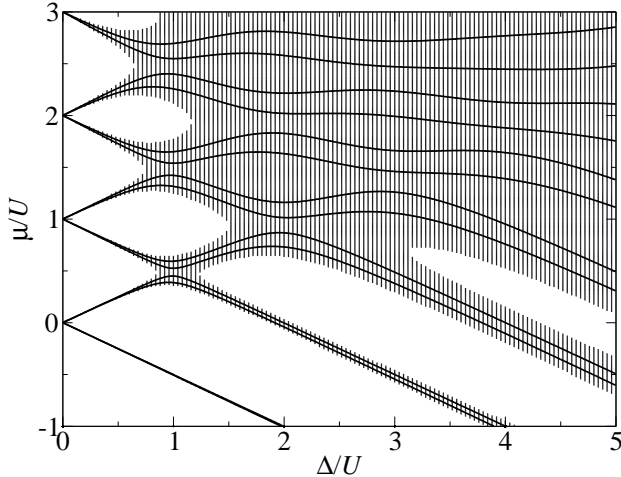


FIG. 20: The phase diagram of the dimer chain at $J/\Delta = 0.05$ for an L -mer containing two dimers. As compared to the single dimer phase diagram at in Fig. 19, we see that the Mott regions are larger, implying the increased stabilization of the Mott phase. This is particularly evident in the bottom-right corner of the figure which shows an additional Mott region with filling $n = 3/2$.

The other qualitative difference in Fig. 20 concerns the N -domains which are doubled in number as compared to those shown in Fig. 19. Depending on the value of μ the ground state of the Hamiltonian in (75) can have $N = 0, 1, 2, \dots$ particles and each of these values appears as a distinct N -domain in Fig. 20. Since $L = 2N_d = 4$, the average number of particles per site in the L -mer is $n = N/4$. The additional N -domains, however, have no qualitative effect on the phase diagram and Mott phases only appear at integral and half-integral values of n . We have performed some additional calculations for $N_d = 3$, that is for L -mers with three dimers. As expected, we find only slightly expanded MI regions resulting from the increased stabilization of the Mott phases.

It is of interest to compare the MSMFT phase diagram with that given in Fig. 17 of Ref. [7] which was obtained using the quantum Monte Carlo (QMC) method. These results can effectively be taken as exact. In terms of our variables, the data in this figure correspond to $J/\Delta = 0.25$, a factor of five larger than the value used in Figs. 19 and 20. Before comparing with the data in Ref. [7], we first note that the extent of the MI regions in the QMC simulations for 1D systems are enhanced significantly as compared to the MSMFT results (as seen, for example, in Fig. 7). In other words, the $\tilde{J}_{\text{cr}}(\tilde{\mu}, \tilde{\Delta})$ surface of the QMC calculations lies considerably above that of the MSMFT calculations. As a result, a direct comparison of the results obtained using the two methods is not particularly meaningful for one and the same fixed value of J/Δ . However, if J/Δ is scaled in proportion to the relative extent of the MI regions, one might expect a correspondence between the two sets of results. This is indeed the case. The results in Fig. 17 of Ref. [7] are qualitatively similar to those of Fig. 21 obtained for $J/\Delta = 0.1$. One obvious qualitative difference is that the MI regions in the MSMFT calculations do not exhibit the pointed shape seen in the QMC results as was found for the case of the homogeneous 1D lattice (see Fig. 7). One can infer from this feature that the QMC version of Fig. 17 would have cusps running along the top of the Mott lobes. Such cusps are absent in higher dimensions.

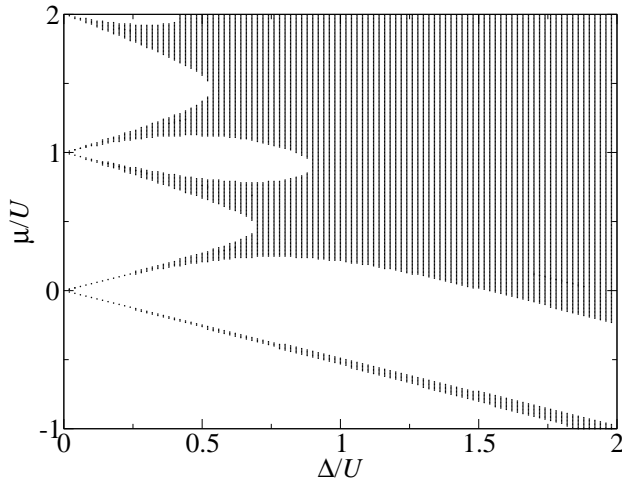


FIG. 21: The phase diagram of the dimer chain at $J/\Delta = 0.1$ for an L -mer containing two dimers. The range of μ/U corresponds to that in Fig. 17 of Ref. [7] (note that their interaction parameter is $U' = U/2$). The lowest unshaded region in the figure is a $n = 0$ Mott insulator.

Finally, it is instructive to consider the variation of the order parameters ψ_A and ψ_B and the on-site densities $\langle \hat{n}_A \rangle$ and $\langle \hat{n}_B \rangle$ as a function of $\tilde{\Delta}$ along the line $\tilde{\mu} = 0.5$ in Fig. 20. The order parameters are determined self-consistently using the iterative scheme in (54). In the MI phase, the order parameters converge to zero and the Hamiltonian \hat{K}_L reduces to the dimer Hamiltonian \hat{K}_L^0 . Thus in the Mott regions, $\langle \hat{n}_A \rangle$ is equal to $\langle \hat{n}_A \rangle_0$, the value obtained for the ground state of \hat{K}_L^0 , with a similar equality for the B site. In the SF regions, $\langle \hat{n}_A \rangle$ is no longer equal to $\langle \hat{n}_A \rangle_0$ but the latter quantity is still well-defined and it is of interest to compare it with the actual on-site density $\langle \hat{n}_A \rangle$.

In Fig. 22 we plot the on-site densities for the A and B sites terminating the L -mer, as a function of $\tilde{\Delta}$, for $J/\Delta = 0.05$ and $\tilde{\mu} = 0.5$. We first consider $\langle \hat{n}_A \rangle_0$ and $\langle \hat{n}_B \rangle_0$ which are shown by the dashed curves in Fig. 22. Referring to Fig. 20, we see that the $\tilde{\mu} = 0.5$ line remains in the $N = 4$ domain ($n = 1$) for $\tilde{\Delta}$ between 0 and approximately 3. For this range of $\tilde{\Delta}$, $\langle \hat{n}_A \rangle_0$ and $\langle \hat{n}_B \rangle_0$ vary continuously with $\tilde{\Delta}$. For small $\tilde{\Delta}$, they are both close to 1 but as $\tilde{\Delta}$ passes through 1, $\langle \hat{n}_A \rangle_0$ increases continuously to about 2 while $\langle \hat{n}_B \rangle_0$ decreases to about 0. This change in occupation reflects the change in the dimer state from predominantly $|1, 1\rangle$ to $|2, 0\rangle$ as Fig. 16 for $J/\Delta = 0$ would suggest. For larger $\tilde{\Delta}$, the $\tilde{\mu} = 0.5$ line successively enters $N = 5, 6$ and 7 domains. When an N -domain boundary is crossed, the densities $\langle \hat{n}_A \rangle_0$ and $\langle \hat{n}_B \rangle_0$ calculated for the ground state of \hat{K}_L^0 change discontinuously. On entering the $N = 5$ domain, $\langle \hat{n}_A \rangle_0$ jumps approximately to 2.25 (the occupancy of the interior A -site jumps to about 2.75). When the $N = 6$ domain is entered, $\langle \hat{n}_A \rangle_0$ jumps to approximately 3. The latter indicates that the \hat{K}_L^0 ground state now has predominantly the $|3, 0\rangle$ configuration.

The full curves in Fig. 22 show the variation of $\langle \hat{n}_A \rangle$ and $\langle \hat{n}_B \rangle$. These quantities generally follow the variation of $\langle \hat{n}_A \rangle_0$ and $\langle \hat{n}_B \rangle_0$, respectively, and, as stated earlier, are equal to the latter in the MI phases where $\langle \psi_A \rangle$ and $\langle \psi_B \rangle$ are zero. Unlike $\langle \hat{n}_A \rangle_0$ and $\langle \hat{n}_B \rangle_0$, however, $\langle \hat{n}_A \rangle$ and $\langle \hat{n}_B \rangle$ vary continuously through the SF regions from one MI phase to another since in these regions the ground state of \hat{K}^{MF} is not a number eigenstate. We also find that the densities at the interior A and B sites do not deviate much from the densities at the terminating A and B sites of the

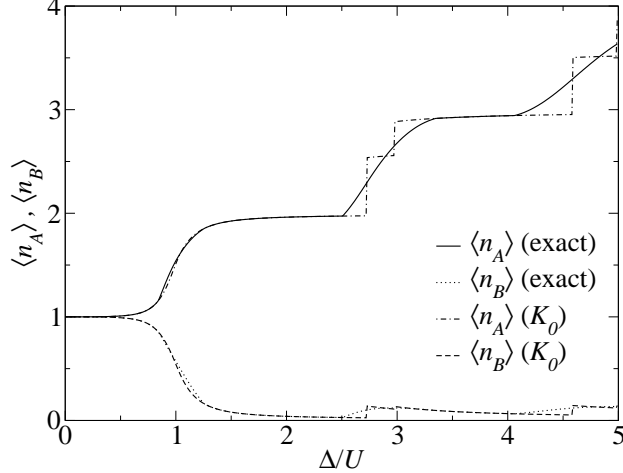


FIG. 22: A plot of the on-site densities for the terminating A and B sites of an L -mer containing two dimers, as a function of $\tilde{\Delta}$, for the values of $J/\Delta = 0.05$ and $\tilde{\mu} = 0.5$. The densities $\langle \hat{n}_A \rangle$ and $\langle \hat{n}_B \rangle$ are obtained from the ground state of the full Hamiltonian (74); for comparison, we also show the densities $\langle \hat{n}_A \rangle_0$ and $\langle \hat{n}_B \rangle_0$ corresponding to the ground state of \hat{K}_L^0 in (75). The discontinuities in $\langle \hat{n}_A \rangle_0$ and $\langle \hat{n}_B \rangle_0$ occur at the boundaries of the N -domains. On the other hand, $\langle \hat{n}_A \rangle$ and $\langle \hat{n}_B \rangle$ vary continuously, but show kinks at the boundaries between the MI and SF phases.

$N_d = 2$ L -mer.

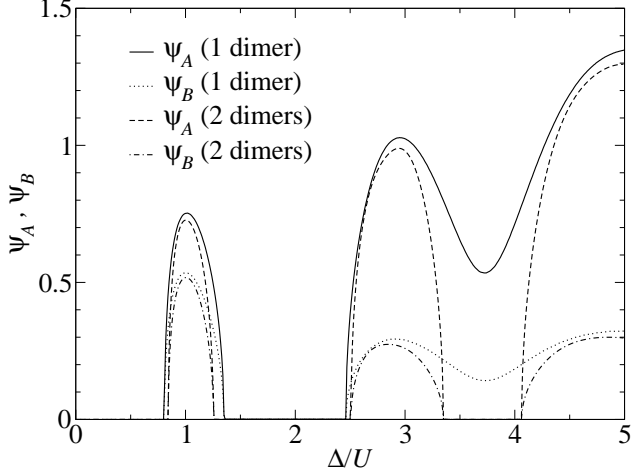


FIG. 23: A plot of the order parameters, ψ_A and ψ_B , as a function of $\tilde{\Delta}$ for $J/\Delta = 0.05$ and $\tilde{\mu} = 0.5$. The order parameters are shown for L -mers containing one and two dimers corresponding to the phase diagrams in Figs. 19 and 20.

In Fig. 23 we plot the order parameters, ψ_A and ψ_B , as a function of $\tilde{\Delta}$ for the same values of $J/\Delta = 0.05$ and $\tilde{\mu} = 0.5$. For comparison, we show the order parameters for both the $N_d = 1$ and $N_d = 2$ L -mers corresponding to Figs. 19 and 20. The $\tilde{\mu} = 0.5$ line passes through two MI regions in the case of $N_d = 1$ where the order parameters are zero, while in the case of $N_d = 2$, the line passes through three MI regions. The proximity of a MI region in the $N_d = 1$ case leads to the dip in the order parameters seen in the range $\tilde{\Delta} \simeq 3.5-4$. With increasing N_d , the MI phase is stabilized and results in the $\tilde{\mu} = 0.5$ scan passing through a MI region for this range of $\tilde{\Delta}$.

In the vicinity of a MI-SF boundary the order parameters are seen to behave as $|\tilde{\Delta} - \tilde{\Delta}_{\text{cr}}|^{1/2}$ which is consistent with the mean-field behaviour given by (32). We also observe that the value of ψ_A is larger than that of ψ_B , implying a larger superfluid fraction on the A -site as compared to the B -site. This is to be expected given the lower on-site energy ε_A . The condensate density ratio $(\psi_B/\psi_A)^2$, however, is somewhat larger than what one might expect on the basis of the on-site densities. For example, at $\tilde{\Delta} = 1$ we have $(\psi_B/\psi_A)^2 \simeq 0.44$ while $\langle \hat{n}_B \rangle / \langle \hat{n}_A \rangle \simeq 0.33$. A similar enhancement of the condensate ratio is observed near $\tilde{\Delta} = 3$ and $\tilde{\Delta} = 5$.

The above results were found for a one-dimensional system, and while one does not expect mean-field theory to represent the exact ground state in this case, it is simplest to demonstrate the application of MSMFT to lattices with a non-monatomic basis in one dimension. We wish to stress, however, that the qualitative behaviour obtained for the dimer chain is also obtained for higher-dimensional lattices. As one example, we have considered the two-dimensional honeycomb lattice in which the site energies within a single hexagon alternate $ABABAB$. The application of MSMFT to this system leads to results which are essentially identical to those obtained for the dimer chain. For a value of $J/\Delta = 0.05$ we find a phase diagram similar to that shown in Fig. 21; the one minor difference is the extent of the various Mott lobes. As for the dimer chain problem, the phase diagram for the two-dimensional lattice can be understood in terms of the N -domain structure shown in Fig. 16.

B. A Superlattice with Loopholes

In all of the examples we have considered so far, the phase diagrams obtained using SDMFT and MSMFT are qualitatively similar. As shown previously by Buonsante *et al.* [15, 17], this is not always the case. In particular, they find that certain superlattices exhibit a so-called ‘loophole’ structure which corresponds to Mott domains that do not arise in SDMFT.

Here we briefly consider an example of this kind. The specific superlattice we study was previously examined using SDMFT [16]. It consists of a four-site superlattice with site energies given by $\epsilon_1 = 1.9\Delta$, $\epsilon_2 = 0.3\Delta$, $\epsilon_3 = 1.3\Delta$, $\epsilon_4 = 0.0\Delta$ with the same hopping parameter J between nearest-neighbour sites and the same on-site interaction U . The phase diagram as determined in SDMFT and MSMFT is shown in Fig. 24. We observe that Mott domains for integral average filling do not arise with SDMFT. However, within MSMFT, these domains are present and have the loophole structure referred to above.

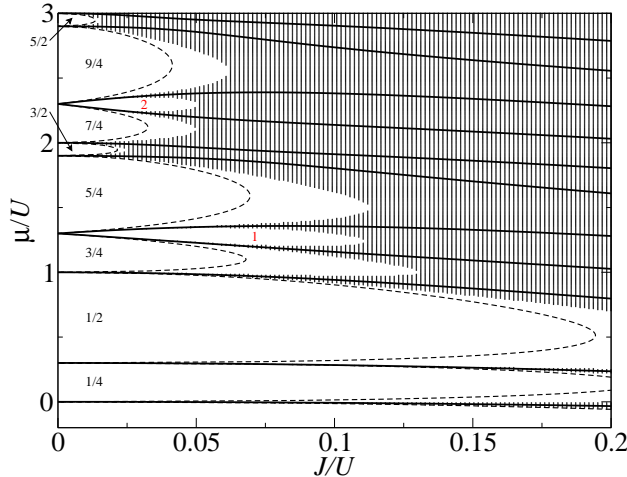


FIG. 24: Phase diagram for a four-site superlattice which exhibits loopholes. The parameters defining the superlattice are given in the text. The shaded region corresponds to the SF phase as determined using MSMFT. The dashed lines show the phase boundaries determined using SDMFT. The numbers n labelling each of the Mott domains is the average filling of the superlattice. We note that new Mott domains appear at $n = 1$ and $n = 2$ within MSMFT. The solid lines show the N -domains for the four-site cluster. Within SDMFT, the N -domains boundaries are straight lines, parallel to the J/U axis, which start at the edges of the Mott domains along the μ/U axis.

The origin of the integral- n loopholes is associated with degeneracies of different particle configurations in the atomic limit ($J \rightarrow 0$). Denoting the $\hat{K}_L^0(J=0)$ eigenstates as $|n_1, n_2, n_3, n_4\rangle$, the $N=4$ configurations $|0, 2, 0, 2\rangle$ and $|0, 1, 1, 2\rangle$ have the same energy of $E_4 = 2.6U$. As the chemical potential μ is swept through $E_4 - E_3 = 1.3U$, the particle number in the system jumps by 2. This explains the absence of a $n = 1$ Mott domain along the $J/U = 0$ axis. As J/U increases, the degeneracy between the two $N = 4$ configurations is lifted within MSMFT and a $n = 1$ region becomes accessible for the formation of a Mott domain. Such a Mott domain does indeed form as seen in Fig. 24. Within SDMFT, the degeneracy persists since $\hat{K}_L^0(J=0)$ is used in the perturbation analysis for all J . As a result, the $n = 1$ Mott domain does not appear. A similar argument applies to the $n = 2$ Mott domain. Underlying its formation is the degeneracy of the $|1, 3, 1, 3\rangle$ and $|1, 2, 2, 3\rangle$ $N = 8$ states in the atomic limit.

More generally, qualitative differences between SDMFT and MSMFT may be found whenever degeneracies of the kind discussed above appear in the ground states of the $\hat{K}_L^0(J=0)$ grand Hamiltonian. Such degeneracies appear in

all of the examples of loopholes considered previously [15, 17]. They also arise in models dealing with two bosonic species [22] and one can expect differences between SDMFT and MSMFT to appear in these cases as well.

V. CONCLUSIONS

In this paper we have developed, explained and utilized a mean-field theory of the Mott insulator-superfluid transition of bosons moving in optical lattices. In this approach, the lattice is partitioned into clusters which we refer to as L -mers. In the Bose-Hubbard model the L -mers are coupled by the hopping Hamiltonian; they can be isolated by invoking a mean-field decoupling procedure whereby a superfluid order parameter is introduced for all boundary sites of the L -mer. This leads to a mean-field Hamiltonian taking the form shown in Eq. (12). The resulting theory is thus a multi-site mean-field theory (MSMFT); it should be contrasted with site-decoupled mean-field theories which allow for different order parameters at different sites [22] but neglect inter-site correlations.

The ground state of the mean-field Hamiltonian defines a grand potential energy functional of the various order parameters. The stationary points of this functional are shown to correspond to self-consistent solutions in that the order parameters evaluated at the stationary point coincide with the order parameters defining the mean-field Hamiltonian itself. A detailed analysis reveals that the stationary points are, in general, *saddle points*. As a result, they cannot be located by minimizing the energy functional. For weak hopping there is only one self-consistent solution, the Mott insulating phase, whereas at larger hopping a second stationary point appears with lower energy, corresponding to the superfluid phase.

The identification of the phase boundaries separating the Mott insulating and superfluid phases can be analyzed using perturbation theory. Our work has clarified the relationship between two different criteria for the determination of the phase boundaries, one based on the energy functional itself and the second based on the stability of an iterative map. We show that the two criteria are equivalent and can be used interchangeably.

We have applied our theory to the Bose-Hubbard model for d -dimensional hypercubic lattices, for $d = 1$ (chains), $d = 2$ (square lattice), and $d = 3$ (simple cubic lattice). Our results demonstrate the improvements that MSMFT affords relative to site-decoupled mean-field theories. This, of course, is what one expects since the theory becomes exact in the limit of an infinite L -mer. Specifically, our numerical results make clear that as the size of the L -mer *and* the dimensionality of the system are increased, better agreement between MSMFT and numerical Monte Carlo data is obtained. However, mean-field theories typically underestimate the stability of the Mott insulating phase, and therefore (for a given chemical potential) underestimate the critical hopping at which this phase becomes unstable with respect to the superfluid phase.

In addition, we have applied our MSMFT to the analysis of one-dimensional superlattices. For the dimer chain, the inequivalence of the two sites within the dimer necessitates the introduction of two order parameters. The stationary points of the resulting energy functional are found to be saddle points in this case. Apart from the underestimation of the critical hopping mentioned above, the phase boundaries we obtain are in qualitative agreement with those obtained on the basis of Monte Carlo simulations [7]. We also considered one example of a more complex superlattice for which the predictions of SDMFT and MSMFT differ qualitatively. Specifically, the phase diagram as determined using MSMFT exhibits loopholes which are absent in SDMFT. Such qualitative differences are expected to arise when degeneracies exist in the $\hat{\mathcal{K}}_L^0(J=0)$ ground state energy.

The MSMFT was used previously in a study of the disordered Bose-Hubbard model [13], and will be applied to other, more complicated situations in subsequent work.

APPENDIX

A practical limitation of the MSMFT is the size of the Hilbert space needed to diagonalize the mean-field Hamiltonians $\hat{\mathcal{K}}_L^0$ and $\hat{\mathcal{K}}^{MF}$ which grows exponentially with the size of the L -mer. A natural basis is provided by the occupation number states $|\{n_l\}\rangle$ where $l = 1, \dots, L$ and $n_l = 0, 1, \dots, \infty$. For a given average number of particles per site, it is sufficient to truncate the range of n_l at some maximum number n_{max} which can be varied to ensure convergence of the eigenstate calculations. Within this truncated basis, the dimension of the basis is S^L where $S = n_{max} + 1$.

The perturbative calculations require the ground state of $\hat{\mathcal{K}}_L^0$ for N particles and excited states for $N \pm 1$ particles. The truncated basis discussed above is excessive since it includes states with different total particle numbers. To obtain the eigenstates within an N -particle subspace we therefore retain only those states with the required number of particles. We denote the states in this subset as $|k\rangle$, $k = 1, \dots, N_{st}$, where N_{st} is the number of states in the set. These states are the occupation number states satisfying $\sum_{l=1}^L n_l = N$ with $n_l \leq n_{max}$.

We now discuss how the size of the basis set can be reduced further with the use of group theory [43]. To be specific, we consider the 3×3 L -mer illustrated in Fig. 2(b). The symmetry operations which leave the L -mer invariant define

a group \mathcal{G} of order g ($g = 8$ in this case) with group elements G_m consisting of the identity, three rotations and four reflections. The savings provided by group theory stem from the fact that the Hamiltonian $\hat{\mathcal{K}}_L^0$ commutes with the group elements G_m and that the ground state $|0\rangle$ of the L -mer belongs to the identity irreducible representation with the property $G_m|0\rangle = |0\rangle$. The reduced energy matrix in (57) involves matrix elements of the form $\langle \nu | \sum_{l \in A} (\hat{a}_l^\dagger + \hat{a}_l) |0\rangle$. We observe that

$$\begin{aligned} G_m \sum_{l \in A} (\hat{a}_l^\dagger + \hat{a}_l) |0\rangle &= G_m \sum_{l \in A} (\hat{a}_l^\dagger + \hat{a}_l) G_m^{-1} G_m |0\rangle \\ &= G_m \sum_{l \in A} (\hat{a}_l^\dagger + \hat{a}_l) G_m^{-1} |0\rangle \\ &= \sum_{l \in A} (\hat{a}_l^\dagger + \hat{a}_l) |0\rangle. \end{aligned} \quad (84)$$

The last step is a consequence of the invariance of the sum of field operators under a symmetry operation. The state $\sum_{l \in A} (\hat{a}_l^\dagger + \hat{a}_l) |0\rangle$ thus belongs to the identity representation and as a result, the state $|\nu\rangle$ must also belong to this representation for the matrix element to be finite. It is clear from this discussion that the calculation of the matrix in (25) cannot be simplified using group theory since the action of \hat{c}_α on $|0\rangle$ creates a state that belongs to other irreducible representations.

Since $|\nu\rangle$ must belong to the identity representation, it can be expanded in terms of states belonging to this representation. These states are constructed as follows,

$$|\kappa\rangle = \frac{1}{\sqrt{N_\kappa}} \sum_{m=1}^g G_m |k\rangle, \quad (85)$$

where $1/\sqrt{N_\kappa}$ is an appropriate normalization constant. The number of distinct states formed in this way is $N_{sym} < N_{st}$. This reduction in the dimension of the basis set is the advantage afforded by the use of group theory.

Within this symmetrized basis, an eigenstate of $\hat{\mathcal{K}}^0$ is expanded as

$$|\nu\rangle = \sum_{\kappa=1}^{N_{sym}} c_\kappa^{(\nu)} |\kappa\rangle. \quad (86)$$

The expansion coefficients and corresponding eigenvalues $\Omega_\nu(\{0\})$ are then obtained by the diagonalization of the Hamiltonian matrix $\langle \kappa | \hat{\mathcal{K}}_L^0 | \kappa' \rangle$. The reduction of the dimension of the eigenvalue problem from N_{st} to N_{sym} is roughly a factor g , the order of the group, and represents a significant computational saving. However, even with the use of group theory, the 4×4 L -mer for a 2D square lattice remains a formidable calculation.

Acknowledgments

This work was supported by grants from the Natural Sciences and Engineering Research Council of Canada. We would also like to thank Vittoria Penna for useful discussions.

- [1] M.P.A. Fisher, P.B. Weichman, G. Grinstein and D.S. Fisher, Phys. Rev. B **40**, 546 (1989).
- [2] D. Jaksch, C. Bruder, J.I. Cirac, C.W. Gardiner, and P. Zoller, Phys. Rev. Lett. **81**, 3108 (1998).
- [3] M. Greiner, O. Mandel, T. Esslinger, T.W. Hänsch and I. Bloch, Nature **415** 39 (2002)
- [4] G. G. Batrouni and R. T. Scalettar, Phys. Rev. B **46**, 9051 (1992).
- [5] J. K. Freericks and H. Monien, Phys. Rev. B **53**, 2691 (1996).
- [6] T. D. Kühner and H. Monien, Phys. Rev. B **58**, R14741 (1998).
- [7] V.G. Rousseau, D.P. Arovas, M. Rigol, F. Hebert, G.G. Batrouni, and R.T. Scalettar, Phys. Rev. B **73**, 174516 (2006).
- [8] B. Capogrosso-Sansone, N. V. Prokof'ev and B. V. Svistunov, Phys. Rev. B **75**, 134302 (2007).
- [9] B. Capogrosso-Sansone, S. G. Söyler, N. Prokof'ev and B. Svistunov, Phys. Rev. A **77**, 015602 (2008).
- [10] N. Teichmann, D. Hinrichs, M. Holthaus and A. Eckardt, Phys. Rev. B **79**, 100503(R) (2009).
- [11] F.E.A. dos Santos and A. Pelster, Phys. Rev. A **79**, 013614 (2009).
- [12] U. Bissbort, R. Thomale, and W. Hofstetter, Phys. Rev. A **81**, 063643 (2010).

- [13] P. Pisarski, R.M. Jones and R.J. Gooding, Phys. Rev. A **83**, 053608 (2011).
- [14] R. Roth and K. Burnett, Phys. Rev. A **68**, 023604 (2003).
- [15] P. Buonsante, V. Penna, and A. Vezzani, Phys. Rev. A **70**, 061603 (2004).
- [16] P. Buonsante and A. Vezzani, Phys. Rev. A **70**, 033608 (2004).
- [17] P. Buonsante, V. Penna, and A. Vezzani, Laser Phys. **15**, 361 (2005).
- [18] P. Buonsante and A. Vezzani, Phys. Rev. A **72**, 013614 (2005).
- [19] X. Deng, R. Citro, A. Minguzzi and E. Orignac, Phys. Rev. A **78**, 013625 (2008).
- [20] I. Hen and M. Rigol, Phys. Rev. B **80**, 134508 (2009).
- [21] I. Hen, M. Iskin and M. Rigol, Phys. Rev. B **81**, 064503 (2010).
- [22] B.-L. Chen, S.-P. Kou, Y. Zhang and S. Chen, Phys. Rev. A **81**, 053608 (2010).
- [23] A. A. Svidzinsky and S. T. Chui, Phys. Rev. A **68**, 043612 (2003).
- [24] S. Tsuchiya, S. Kurihara and T. Kimura, Phys. Rev. A **70**, 043628 (2004).
- [25] M. Rizzi, D. Rossini, G. De Chiara, S. Montangero and R. Fazio, Phys. Rev. Lett. **95**, 240404 (2005).
- [26] A.B. Kuklov, N. Prokof'ev and B.V. Svistunov, Phys. Rev. Lett. **92**, 050402 (2004).
- [27] A. Isacsson, M.-C. Cha, K. Sengupta and S.M. Girvin, Phys. Rev. B **72**, 184507 (2005).
- [28] M. Iskin, Phys. Rev. A **82**, 033630 (2010).
- [29] A. Isacsson and S. M. Girvin, Phys. Rev. A **72**, 053604 (2005).
- [30] J. Larson, A. Collin, and J.-P. Martikainen, Phys. Rev. A **79**, 033603 (2009).
- [31] A. Mering and M. Fleischhauer, Phys. Rev. A **83**, 063630 (2011).
- [32] K. Sheshadri, H.R. Krishnamurthy, R. Pandit, and T.V. Ramakrishnan, Europhys. Lett. **22**, 257 (1993).
- [33] D. van Oosten, P. van der Straten, and H.T.C. Stoof, Phys. Rev. A **63**, 053601 (2001).
- [34] SDMFT for a homogenous lattice is recovered by noting that the index α takes only one value and that $g = z$, the number of nearest neighbours in the lattice.
- [35] D. S. Rokhsar and B. G. Kotliar, Phys. Rev. B **44**, 10328 (1991).
- [36] W. Krauth, M. Caffarel and J.-P. Bouchaud, Phys. Rev. B **45**, 3137 (1992).
- [37] P. Jain and C. W. Gardiner, J. Phys. B: At. Mol. Opt. Phys. **37**, 3649 (2004).
- [38] S.Q. Zhou and D.M. Ceperley, Phys. Rev. A **81**, 013402 (2010).
- [39] L. D. Landau and E. M. Lifshitz, *Statistical Physics, Part 1*, (Butterworth-Heinemann, 1980).
- [40] See, e.g., D.D. Johnson, Phys. Rev. B **38**, 12807 (1988).
- [41] R.P. Brent, *Algorithms for Minimization without Derivatives*, Chapter 4 (Prentice-Hall, Englewood Cliffs, 1973).
- [42] The parameters are obtained by a nonlinear fit of $\ln \bar{C}_l(L)$ to the logarithm of (69).
- [43] For an example of the use of group theory in lattice calculations, see G. Fano, F. Ortolani and A. Parola, Phys. Rev. B **46**, 1048 (1992).